

Phase-field boundary conditions for the voxel finite cell method: surface-free stress analysis of CT-based bone structures

L. H. Nguyen¹, S. K. F. Stoter¹, T. Baum², J. S. Kirschke²,
M. Ruess³, Z. Yosibash⁴, and D. Schillinger^{1,*}

¹*Department of Civil, Environmental, and Geo-Engineering, University of Minnesota, Minneapolis, USA*

²*Department of Neuroradiology, Klinikum rechts der Isar, Technische Universität München, Munich, Germany*

³*School of Engineering, University of Glasgow, United Kingdom*

⁴*Department of Mechanical Engineering, Ben-Gurion-University of the Negev, Beer Sheva, Israel*

SUMMARY

The voxel finite cell method employs unfitted finite element meshes and voxel quadrature rules to seamlessly transfer CT data into patient-specific bone discretizations. The method, however, still requires the explicit parametrization of boundary surfaces to impose traction and displacement boundary conditions, which constitutes a potential roadblock to automation. We explore a phase-field based formulation for imposing traction and displacement constraints in a diffuse sense. Its essential component is a diffuse geometry model generated from metastable phase-field solutions of the Allen-Cahn problem that assumes the imaging data as initial condition. Phase-field approximations of the boundary and its gradient are then employed to transfer all boundary terms in the variational formulation into volumetric terms. We show that in the context of the voxel finite cell method, diffuse boundary conditions achieve the same accuracy as boundary conditions defined over explicit sharp surfaces, if the inherent length scales, i.e., the interface width of the phase-field, the voxel spacing and the mesh size, are properly related. We demonstrate the flexibility of the new method by analyzing stresses in a human femur and a vertebral body.

Copyright © 2016 John Wiley & Sons, Ltd.

Received . . .

KEY WORDS: Voxel finite cell method; phase-fields; diffuse boundary methods; patient-specific simulations; femur; vertebra

*Correspondence to: Dominik Schillinger, Department of Civil, Environmental, and Geo-Engineering, University of Minnesota, 500 Pillsbury Drive S.E., Minneapolis, MN 55455, USA; Phone: +1 612 624-0063; Fax: +1 612 626 7750; E-mail: dominik@umn.edu

CONTENTS

1	Introduction	3
2	The voxel finite cell method	4
2.1	Discretization with non-boundary-fitted elements	4
2.2	Quadrature based on recursive subdivision	5
2.3	Quadrature based on rasterized voxel data	5
3	Diffuse geometry and phase-field approximations	6
3.1	Phase-field approximation of volume and surface integrals	7
3.2	An initial boundary value problem based on the Allen-Cahn equation	8
3.3	Discretization in space and time	9
3.4	Transferring imaging data into phase-fields	10
4	A phase-field approach for the surface-free imposition of boundary conditions	11
4.1	Neumann boundary conditions	11
4.2	Dirichlet boundary conditions	11
4.3	Imaging data vs. phase-fields: the link back to the voxel finite cell method	12
4.4	3D benchmark: a spherical thick shell	13
4.5	Relating phase-field length scale, voxel spacing, and mesh size	16
4.6	Implementation aspects	16
5	Patient-specific bone strength analysis without explicit geometry reconstruction	17
5.1	Femur	17
5.1.1	Discretization with the voxel finite cell method.	18
5.1.2	Loading on sharp explicit surfaces.	18
5.1.3	Loading on diffuse implicit phase-fields.	19
5.1.4	Validation and comparison.	20
5.2	Vertebra	21
5.2.1	Imaging data and material properties.	24
5.2.2	Diffuse phase-field representations of upper and lower faces.	24
5.2.3	Analysis of the upper half of the vertebra.	25
5.2.4	Analysis of the full vertebral body.	27
6	Summary and conclusions	28
	Appendix	30
A-1	Neumann boundary conditions	30
A-2	Dirichlet boundary conditions	31

1. INTRODUCTION

Due to the intricate process of transferring diagnostic imaging data into patient-specific models, simulation workflows involving complex physiological geometries largely rely on the manual intervention of specially trained analysts. This constitutes a significant roadblock for a wider adoption of predictive simulation in clinical practice, as the associated cost and response times are incompatible with tight budgets and urgent decision-making. A prominent example is bone strength analysis via image-based finite element simulations [1]. Many clinical studies have shown that results of finite element simulations are able to increase the fidelity of fracture risk prediction [2, 3, 4] or can help surgeons optimize postfracture follow-up care [5, 6]. However, using high-resolution computed tomography (CT) scans to run diagnostic simulations in clinical practice is currently obstructed by the effort of building patient-specific computational models.

Voxel finite element methods [7, 8, 9, 10] provide a potential pathway to overcome this difficulty. They associate each voxel (or a group of voxels) of a CT scan with one linear hexahedral element. In combination with appropriate constitutive laws, e.g., based on plasticity or damage mechanics [11], voxel finite elements have been shown to accurately predict the evolution of bone failure [12]. However, they involve a prohibitive computational expense when applied to CT scans of a complete bone. The voxel finite cell method [13, 14, 15, 16] applies a similar concept, but at a significantly reduced computational cost. The voxel finite cell method approximates the solution fields on a simple mesh that does not have to conform to the geometric boundaries of the object to be analyzed. Instead, the geometry is captured implicitly by means of special voxel-based quadrature rules. This eliminates the need for boundary conforming meshes and opens the door for a seamless integration of patient-specific imaging data into finite element analysis.

The voxel finite cell method has been applied for patient-specific bone simulations in the linear elastic range [13, 14, 15], including stochastic analyses and uncertainty quantification [16], phase-field fracture [17] and coupled bone/implant simulations for post-fracture care [18]. It directly operates on imaging data in the form of volumetric pixels (voxels) derived from computed tomography (CT) scans. The voxel finite cell method finds the location of each quadrature point in the voxel model and derives the material stiffness at this particular point based on the Hounsfield Unit (HU) value [19, 20], including the case of zero stiffness if the quadrature point is located outside the bone. Thus, bone geometry and heterogeneous material properties are implicitly accounted for during integration of the stiffness matrix. This procedure can also be interpreted as a direct homogenization strategy [21]. In the context of bone mechanics, validation studies have confirmed the accuracy of the finite cell method [15], showing excellent correlation with strains and displacements obtained from in-vitro experiments and boundary-fitted high-order finite element analysis [22, 23, 24].

The voxel finite cell method still requires the reconstruction of an explicit parametrization of boundary surfaces within the embedding finite element mesh in order to impose boundary conditions. Such a segmentation is difficult to automate, relying the intervention of a specially trained analyst. In this paper, we describe a new strategy that enables the voxel finite cell method to circumvent explicit surface parametrization. It is based on a diffuse boundary approach that leverages the Dirac δ property of a phase-field gradient to impose boundary conditions in a diffuse sense. Its combination with the voxel finite cell method results in a method that is able to directly operate on imaging data, completely avoiding a transfer of implicit voxel-based bone geometry into explicit volume and surface parametrizations.

Finite element methods based on diffuse boundaries [25, 26, 27, 28], also known as diffuse domain or phase-field methods, offer an approach for solving boundary value problems on very complex domains. Their essential idea is to abandon the concept of sharply defined boundaries and instead approximate the domain implicitly by a phase-field function, which smoothly transitions from one inside the domain to zero in the exterior. The diffusiveness of the geometry approximation, i.e. the local slope of the phase-field at the boundary, is controlled by a characteristic length-scale parameter ε . The phase-field approximation of the boundary and its gradient are then employed to reformulate the boundary value problem on an extended regular domain, very much in the same way

as the finite cell method [29, 30]. The difference is that boundary conditions originally formulated via surface terms are now transferred into additional volumetric source terms, which completely eliminates the need for explicit boundary parametrizations. The concept has a long history [31, 32] and various instantiations of phase-field methods have been published, e.g., for advection-diffusion problems [33, 34], multi-phase flow [35, 36], the evolution of complex cracks [37, 38, 39, 40], fluid vessel networks [41, 42] and phase transition and segregation processes [43, 44, 45].

Our article is organized as follows: Section 2 provides a brief review of the voxel finite cell method. Section 3 describes a methodology for obtaining a suitable phase-field description of an imaging-based geometry via solving an Allen-Cahn problem. Section 4 describes diffuse phase-field formulations for the imposition of Neumann and Dirichlet boundary conditions (i.e., loads and displacements). In particular, we examine a benchmark problem to illustrate how different geometry representations based on imaging data, phase-fields and sharp geometry parametrizations affect the accuracy and convergence behavior of the finite cell method. Section 5 illustrates the new method for the image-based stress analysis of bone structures without surface reconstruction. We demonstrate the simplified workflow and the accuracy of the method for the patient-specific analysis of a femur and a vertebra, comparing its results with experimental data and results obtained from finite cell computations with sharp boundaries. Section 6 summarizes key aspects and draws conclusions.

2. THE VOXEL FINITE CELL METHOD

We start with a concise summary of the tetrahedral finite cell method in the context of linear elasticity and voxel geometries. For details on the tetrahedral finite cell method, we refer the interested reader to the recent contributions in [17, 18, 46]. We note that the original variant of the finite cell method introduced by PARVIZIAN, DÜSTER and RANK [29, 30] has been based on non-boundary-fitted Cartesian meshes with higher-order approximation of the solution fields and adaptive quadrature of intersected elements based on recursive subdivision. A concise summary of the Cartesian finite cell method can be found for example in the review in [47].

2.1. Discretization with non-boundary-fitted elements

The starting point is the variational form, defined on a domain Ω with Dirichlet and Neumann boundaries Γ_D and Γ_N , respectively. For linear elasticity, we use the principle of virtual work

$$\delta W(\mathbf{u}, \delta \mathbf{u}) = \int_{\Omega} \boldsymbol{\sigma} : \delta \boldsymbol{\varepsilon} \, d\Omega - \int_{\Omega} \delta \mathbf{u} \cdot \mathbf{b} \, d\Omega - \int_{\Gamma_N} \delta \mathbf{u} \cdot \mathbf{t} \, d\Gamma_N = 0 \quad (1)$$

where \mathbf{u} and $\delta \mathbf{u}$ are the true and virtual displacements, $\boldsymbol{\sigma}$ and $\delta \boldsymbol{\varepsilon} = 1/2(\nabla \delta \mathbf{u} + \nabla \delta \mathbf{u}^T)$ denote the Cauchy stress and virtual strain tensors, and \mathbf{b} and \mathbf{t} are body forces and boundary traction.

In contrast to the standard finite element method, the finite cell method allows the discretization of (1) with basis functions that can arbitrarily overlap the domain boundary Γ . This concept leads to a non-boundary-fitted finite element mesh, whose elements can be arbitrarily intersected

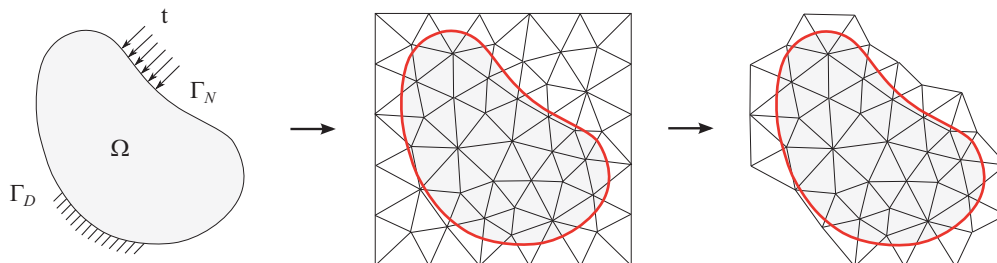


Figure 1. Boundary value problem defined on Ω and its discretization with a non-boundary-fitted triangular mesh, leading to elements intersected by the embedded boundary (in red).

by the domain boundary (see Fig. 1) and constitutes a significant simplification for meshing geometrically complex domains. It is independent of a specific type of finite element basis and has been successfully applied with integrated Legendre functions [29, 30], splines [48, 49], and polyhedral functions [50]. We first define an embedding domain of simple geometry that can be meshed easily and subsequently remove all elements without support in the physical domain.

To enforce Dirichlet boundary conditions at embedded surfaces, the finite cell method uses Nitsche-type methods [51, 52, 53, 54], which do not introduce additional unknowns and preserve a positive definite stiffness matrix. We note that the embedded boundary is still required to be explicitly described by a sharp surface (see the red line in Fig. 1). The Nitsche method extends the principle of virtual work (1) as follows: Find the displacements \mathbf{u} such that $\delta W_{\mathcal{K}} = \delta W_{\mathcal{f}}$, where

$$\delta W_{\mathcal{K}}(\mathbf{u}, \delta \mathbf{u}) = \int_{\Omega} \boldsymbol{\sigma} : \delta \boldsymbol{\varepsilon} \, d\Omega - \int_{\Gamma_D} \mathbf{u} \cdot (\delta \boldsymbol{\sigma} \cdot \mathbf{n}) \, d\Gamma - \int_{\Gamma_D} (\boldsymbol{\sigma} \cdot \mathbf{n}) \cdot \delta \mathbf{u} \, d\Gamma + \beta \int_{\Gamma_D} \mathbf{u} \cdot \delta \mathbf{u} \, d\Gamma \quad (2)$$

$$\delta W_{\mathcal{f}}(\delta \mathbf{u}) = \int_{\Omega} \mathbf{b} \cdot \delta \mathbf{u} \, d\Omega - \int_{\Gamma_D} \hat{\mathbf{u}} \cdot (\delta \boldsymbol{\sigma} \cdot \mathbf{n}) \, d\Gamma + \int_{\Gamma_N} \mathbf{t} \cdot \delta \mathbf{u} \, d\Gamma + \beta \int_{\Gamma_D} \hat{\mathbf{u}} \cdot \delta \mathbf{u} \, d\Gamma \quad (3)$$

Function $\hat{\mathbf{u}}$ denotes the prescribed displacements along the Dirichlet boundary Γ_D and \mathbf{n} is the outward unit normal vector on Γ_D . The method requires a stabilization parameter β that can be determined empirically or by solving a generalized eigenvalue problem [52, 53].

2.2. Quadrature based on recursive subdivision

Elements intersected by the embedded boundary require special numerical integration methods, because the volume integrals in (2) and (3) are only defined over portions of the element domain. If the domain is given explicitly by a geometric model with a sharply defined boundary representation, the finite cell method uses a quadrature technique based on recursive octree subdivision. In the tetrahedral finite cell method, its basic building block is the split of a tetrahedron into eight tetrahedral sub-cells as shown in Fig. 2. This split can be applied recursively for each cut sub-cell until a predefined maximum level of sub-cells is reached. In each sub-cell, a standard 5-point monomial rule for quadratic basis functions and an 11-point quadrature rule for cubic basis functions is used [55], so that quadrature points aggregate at the embedded boundary. The weights of the quadrature points in each sub-cell are scaled with the volume of the sub-cell. The concept of recursive subdivision is illustrated in Fig. 3 for a cube discretized by unfitted tetrahedra. The finite cell method in this form shifts the effort from geometry reconstruction and meshing to numerical quadrature of intersected elements.

2.3. Quadrature based on rasterized voxel data

The layers of images obtained from CT scans of a bone structure can be transferred into a 3D rasterized voxel model, where each voxel contains a Hounsfield Unit (HU) associated with bone

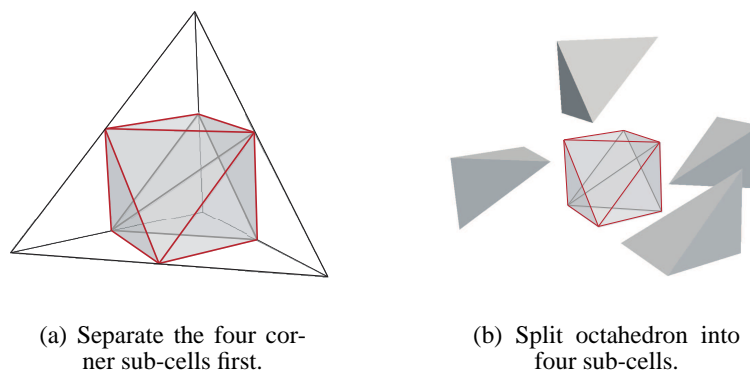


Figure 2. Building block of the recursive subdivision approach: a tetrahedron is split into 8 sub-cells.

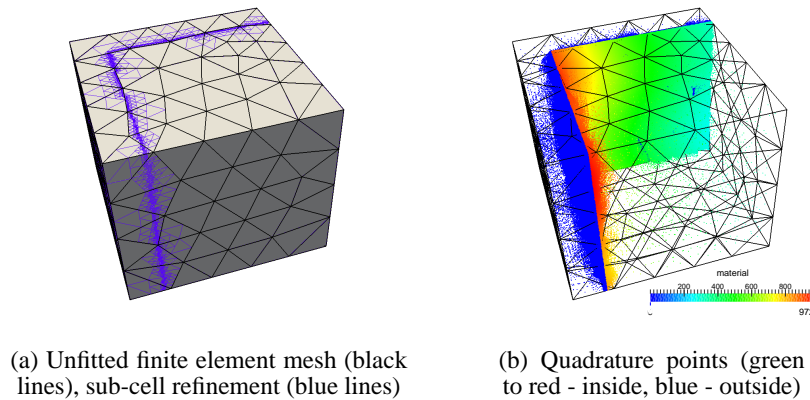


Figure 3. Recursive subdivision quadrature of a boundary representation: The intersecting geometry is captured by aggregating quadrature points along the sharply defined boundary surface.

mineral density (BMD). The BMD can be further associated to the Young's modulus. The resolution of a voxel model can be characterized by a length scale Δ associated with the maximum grid spacing. For the analysis of voxel models, the concept of intersected elements does not apply, as there exists no sharply defined boundary of the problem domain. Instead, we follow the voxel quadrature principles outlined in [17]. First, tetrahedral elements that are completely located outside the physical domain, that is, the HU of all voxels located within this element are below a predefined threshold, are removed from the mesh. Second, we subdivide all remaining tetrahedral elements into sub-cells. The sub-cell resolution is chosen such that the density of the resulting quadrature points sufficiently reflects the stiffness variation of the voxel model. The concept of voxel quadrature in the context of the tetrahedral finite cell method is illustrated in Fig. 4.

3. DIFFUSE GEOMETRY AND PHASE-FIELD APPROXIMATIONS

In this section, we derive diffuse boundary formulations in the context of linear elasticity. We first demonstrate how integrals over a sharply defined domain can be replaced by diffuse integrals formulated in terms of a scalar phase-field function. We also discuss a set of requirements that need to be satisfied by a proper phase-field approximation.

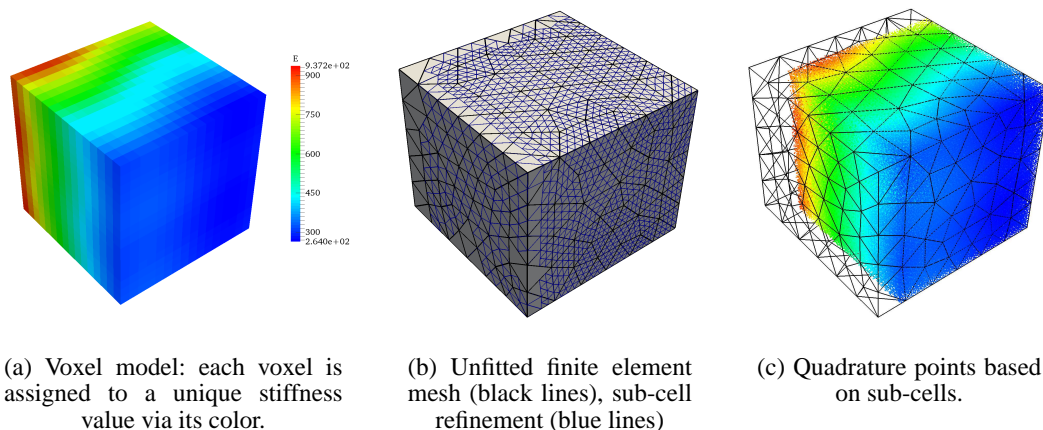


Figure 4. Voxel quadrature: each element is subdivided into quadrature sub-cells, until the stiffness variation of the voxel model with grid spacing Δ is sufficiently resolved by quadrature points.

3.1. Phase-field approximation of volume and surface integrals

The reformulation of the elasticity problem in variational form (2) and (3) can be based on a diffuse representations of the problem domain Ω in terms of a phase-field function c . This phase-field function can be perceived of as a regularized approximation of the Heaviside function H ,

$$H(\mathbf{x}) = \begin{cases} 1.0 & \forall \mathbf{x} \in \Omega \\ 0.0 & \text{otherwise} \end{cases} \quad (4)$$

which represents the sharp boundary limit. Figure 5 illustrates this concept in 1D, showing a Heaviside function with a sharp boundary and diffuse phase-field approximations of different characteristic length scale ε .

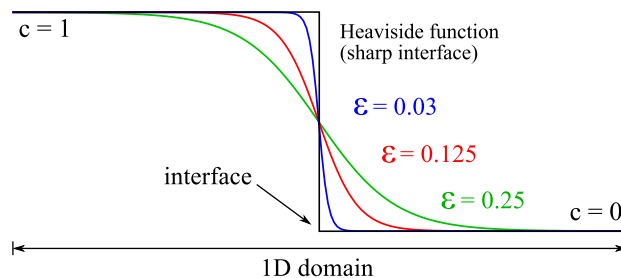


Figure 5. Phase-field c with characteristic length-scale ε for a 1D domain.

We first consider a general volume integral, for which we can write

$$\int_{\Omega} Q \, d\Omega = \int_{\Omega_{em}} Q H \, d\Omega \approx \int_{\Omega_{em}} Q c \, d\Omega \quad (5)$$

where Q is any well-behaved function to be integrated and Ω_{em} denotes an arbitrary embedding domain that fully contains the physical domain Ω . We then consider the diffuse representation of a surface integral

$$\int_{\Gamma} h \, d\Gamma = \int_{\Omega_{em}} h \delta_{\Gamma} \, d\Omega \approx \int_{\Omega_{em}} h |\nabla c| \, d\Omega \quad (6)$$

where the absolute value of the phase-field gradient approximates a Dirac δ distribution at the boundary Γ , that is

$$\delta_{\Gamma} \approx |\nabla c| \quad (7)$$

Figure 6 plots the absolute value of the gradient of the phase-field functions shown in Fig. 5. We observe that a decrease in the diffuse boundary width leads to a contraction of the gradient spike, which centers at the boundary location Γ . To ensure consistent integration of the boundary function h , the absolute value of all phase-field gradient functions must reproduce the key property of a Dirac δ distribution, that is, their integrals across the interface width are equal to 1. This requirement can be expressed concisely as

$$\int_{s_1}^{s_2} \delta_{\Gamma} \, ds = \int_{s_1}^{s_2} \left| \frac{d}{ds} c \right| \, ds = 1 \quad (8)$$

where s is an arbitrary straight line with starting and end points s_1 and s_2 that crosses the diffuse boundary region. In fact, one can easily verify that this property holds for any function that monotonically increases from zero to one (or monotonically decreases from one to zero).

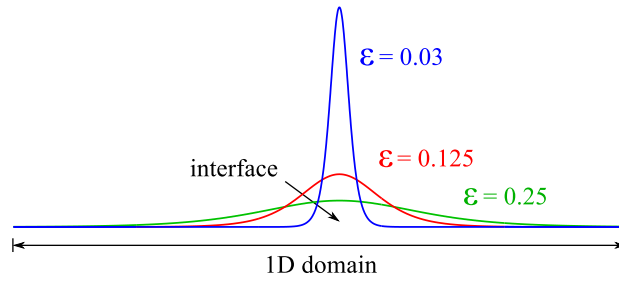


Figure 6. Absolute value of the gradient of the phase-field functions for different length-scales ε .

Many surface integrals require a normal vector. As the surface of the interface will no longer be parametrized explicitly, the normal vector is directly obtained from the implicit phase-field representation as

$$\mathbf{n} \approx -\frac{\nabla c}{|\nabla c|} \quad (9)$$

where \mathbf{n} denotes the outward unit normal along the boundary of the physical domain Ω . This approximation that makes use of the steepest descent property of the gradient allows us to rewrite surface integrals that involve a normal in the following form

$$\int_{\Gamma} \mathbf{q} \cdot \mathbf{n} \, d\Gamma = \int_{\Omega} \mathbf{q} \cdot \mathbf{n} \, \delta_{\Gamma} \, d\Omega \approx -\int_{\Omega} \mathbf{q} \cdot \nabla c \, d\Omega \quad (10)$$

where \mathbf{q} denotes an arbitrary flux quantity.

We finally emphasize that these relations are valid for any phase-field function that satisfies the following four requirements:

1. The phase-field is a monotonically decreasing function from one in the physical domain Ω to zero outside (see Fig. 5).
2. With decreasing length scale parameter ε , the phase-field converges to the Heaviside function described in (4).
3. With decreasing length scale parameter ε and given sufficient smoothness of Γ , the negative normalized gradient of the phase-field converges to the normal of the interface.
4. The diffuse boundary, that is, the spike of the gradient function, centers at the sharp boundary.

In the following sub-section, we will discuss that the phase-field solution obtained from a correctly initialized Allen-Cahn problem satisfies all of these requirements.

3.2. An initial boundary value problem based on the Allen-Cahn equation

We construct suitable auxiliary phase-field functions that are able to implicitly parametrize imaging-based geometries irrespective of their geometric complexity. For the diffuse representation of the boundary Γ , we consider the initial boundary value problem based on the Allen-Cahn equation

$$\frac{\partial c}{\partial t} = \varepsilon^2 \nabla^2 c - \frac{\partial F(c)}{\partial c} \quad \text{on } \Omega_{\text{em}} \times (0, T) \quad (11)$$

$$\nabla c \cdot \mathbf{n} = 0 \quad \text{at } \partial\Omega_{\text{em}} \quad (12)$$

$$c(\mathbf{x}) = H \quad \text{at } t = 0 \quad (13)$$

where $c(x, t)$ represents the phase-field function. Following FENTON et al. [56], we choose the potential function $F(c)$ as a double-well potential

$$F(c) = -\frac{(2c-1)^2}{4} + \frac{(2c-1)^4}{8} = 2c^2(c-1)^2 - \frac{1}{8} \quad (14)$$

with minima at $c = 0$ and $c = 1$. As a result, the phase-field solution c separates into two regions at values zero and one, while the diffusion operator tends to smooth out the spatial discontinuity of c at the interface between these two regions [56, 57] (see also Fig. 5). The balance between double-well potential and the diffusion operator leads to a diffuse boundary region, whose width is controlled by the length-scale parameter ε . In line with the double-well potential, we choose the Heaviside function (4) as the initial condition, which characterizes the sharply defined domain with an explicit boundary surface. The Heaviside function can be directly derived from implicit representations of the geometry, e.g., an analytical expression or imaging data.

With (14), the one-dimensional steady-state phase-field solution of (11) in an infinite half space with boundary $x = a$ is given by

$$c(x) = \frac{1}{2} \left(1 + \tanh \left(\frac{a-x}{\varepsilon} \right) \right) \quad (15)$$

The diffuse functions plotted in Fig. 5 correspond to (15) with different values of ε . It is straightforward to see in the one-dimensional case that functions of the form (15) satisfy all requirements stated above. Phase-fields converge to a Heaviside function with the jump at $x = a$, when ε is decreased. They represent monotonically decreasing functions from zero to one, so that integrating the absolute value of their gradients across the diffuse boundary equals to one for any ε . This can be easily verified as

$$\int_{\Omega} |\nabla c| \, d\Omega = -\frac{1}{2} \left(\tanh \left(\frac{a-x}{\varepsilon} \right) \right) \Big|_{-\infty}^{\infty} = 1 \quad (16)$$

The dynamic behavior of the Allen-Cahn equation has been studied in [57]. Before reaching its steady-state, the solution passes through different evolution phases, each characterized by a certain time scale. In the present scope, we are only interested in the short-term dynamics. At first, given a random initial condition, the forcing associated with $\partial_c F(c)$ dominates the solution behavior, driving the initial data at each point to the closest minimum of the potential (14). As the phase-field values locally approach the two minima, the effect of $\partial_c F(c)$ decreases. At a boundary location, the forcing that wants to form a jump in c starts to compete with the effect of the diffusion term. This finally leads to the formation of a diffuse boundary region instead of a sharp boundary jump. The result is a smooth phase-field function that we adopt as our diffuse geometry model.

It is important to note that these short-term phase-field solutions, also called metastable patterns, are extremely resilient and stable over a long period of time [57]. They therefore constitute a quasi-steady-state solution that can be reliably and efficiently computed. We note that on the long-term time scale, however, diffuse boundaries will eventually start to move and dissipate, leading to either the annihilation of all diffuse boundaries or to one single straight diffuse boundary. While metastable patterns have fully formed at a timescale of order ε^{-1} , the time scale associated with the start of the annihilation and coalescence is at least of order $e^{l/\varepsilon}$, where l corresponds to the smallest distance separating two boundaries [58].

3.3. Discretization in space and time

We discretize the variational weak form of (11) in space with standard nodal finite elements based on linear triangles and tetrahedra and in time with a second-order semi-implicit scheme based on a backward differentiation formula (BDF) and Adams-Bashforth methods [59]. The time-discretized variational form reads

$$\begin{aligned} \frac{1}{2\Delta t} \int (3c^{n+1} - 4c^n + c^{n-1}) \psi \, d\Omega + \\ \varepsilon^2 \int \nabla c^{n+1} \cdot \nabla \psi \, d\Omega + \int (2F'(c^n) - F'(c^{n-1})) \psi \, d\Omega = 0 \end{aligned} \quad (17)$$

where Δt is the time step size, n denotes the current time step, and ψ is a test function. The time integration scheme (17) is simple to implement, second-order accurate and energy-stable for reasonably small time steps (see [59] for the stability criterion).

In practice, we integrate the discretized variational form (17) until a reasonably smooth diffuse boundary has been achieved, following the short-term dynamic behavior of the Allen-Cahn equation discussed above. We assume that we have achieved the metastable state when the 2-norm of the difference between the phase-field solutions at the previous and current time steps falls below a specified fraction of the initial difference between the first two time steps.

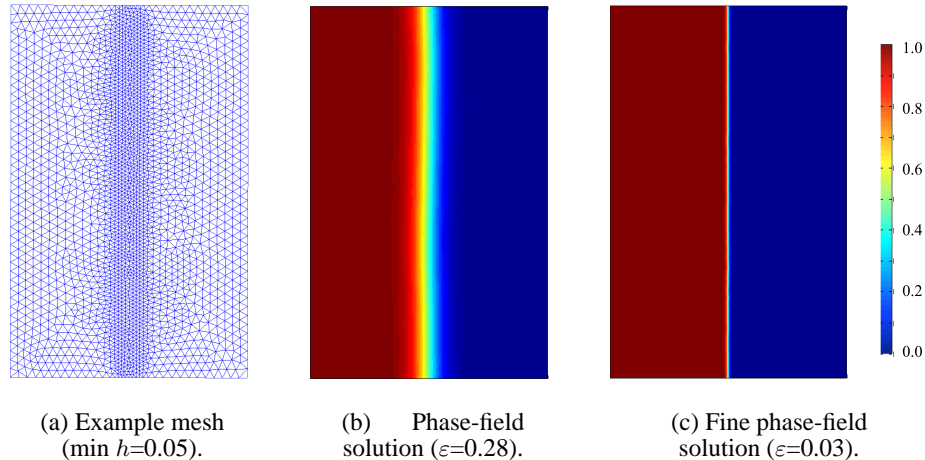


Figure 7. Diffuse geometry example with straight boundary. Phase-field solutions are computed for different length-scale parameters ε on adaptive meshes with minimum local mesh size $h = \varepsilon$.

The width of the diffuse boundary is approximately 4ε [56] and needs to be resolved by a sufficiently fine mesh size in its vicinity. Therefore, the local mesh size h has to be proportional to the length scale ε of the diffuse interface. Figure 7 illustrates the method for a simple geometry with a straight interface. Adaptivity is driven by the criterion to achieve a local mesh size of $h = \varepsilon$ in the vicinity of the diffuse interface.

3.4. Transferring imaging data into phase-fields

In the context of imaging data, we adapt the procedure outlined above to determine a phase-field description c of the implicit voxel model. To this end, we assume the complete domain that is covered by the voxel model as the embedding domain Ω_{em} . We then define a threshold that specifies the distinction between the physical domain Ω of interest and the rest of the domain outside. This yields an initial condition, with which we can solve the Allen-Cahn problem (11) through (14) on a suitable mesh that is adaptively refined at all voxels close to the threshold such that the local element size h corresponds to the characteristic length scale ε of the Allen-Cahn problem.

The phase-field is another implicit representation of the geometry, but in contrast to the voxel model allows the extraction of boundary information in terms of its gradient. Since the boundary in a voxel model is not determined sharply, the phase-field approximation c corresponds to the “data reality” of the original imaging representation.

Figure 8 illustrates the process of transferring imaging data given in terms of a CT scan into a diffuse phase-field representation for a two-dimensional example. We note that in a general setting, unsupervised image processing such as histogram intensity transfers or growing and shrinking algorithms [60] might be required to eliminate noise or small features in the imaging data. For the analysis of bone structures based on CT scans in Section 5, the distinction between a hard tissue and a soft tissue can be made based on the Hounsfield unit (HU). All voxels with a HU above the threshold are defined to be the bone and the ones below are defined as “outside of the bone”. We note that in the scope of this work, we will work with segmented bone data, so that we directly start at the thresholding stage and do not require noise removal.

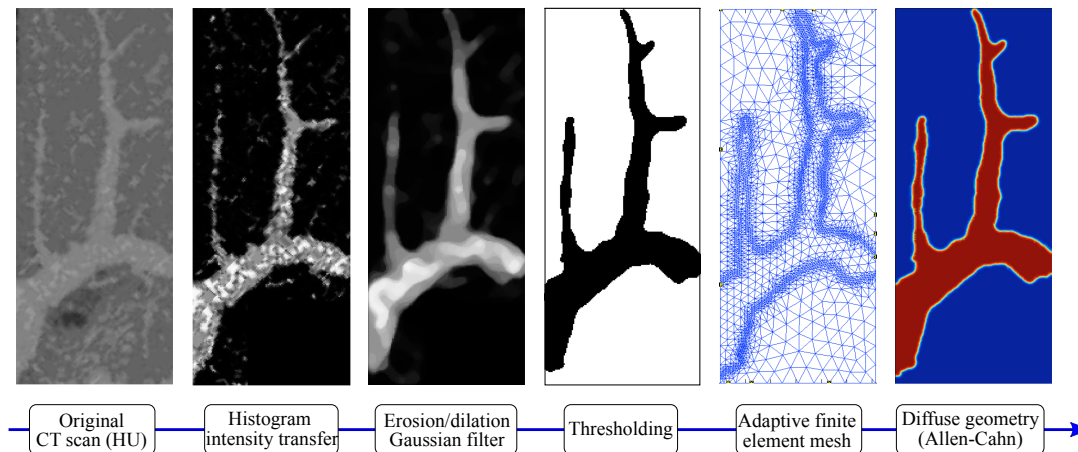


Figure 8. Diffuse geometry example generated from imaging data.

4. A GEOMETRICALLY DIFFUSE PHASE-FIELD APPROACH FOR THE SURFACE-FREE IMPOSITION OF BOUNDARY CONDITIONS

In this section, we derive geometrically diffuse variational formulations in the context of linear elasticity that can be evaluated without surface parametrization. To this end, we replace integrals in the variational formulations shown in Section 2 that are based on sharply defined domains by diffuse integrals, based on the phase-field framework discussed in Section 3. Finally, we link the resulting geometrically diffuse formulations back to the voxel finite cell method.

4.1. Neumann boundary conditions

We first consider the variational formulation (1) that consists of volumetric integrals and a surface integral for the boundary traction at the sharply defined Neumann boundary Γ_N . Assuming a suitable phase-field solution c whose diffuse boundary corresponds to Γ_N , we can employ the identities (5) and (6) to replace integrals over the geometrically exact domain Ω and its sharp boundary Γ_N by integrals over the embedding domain Ω_{em} . The resulting geometrically diffuse variational formulation follows as

$$\delta W(\mathbf{u}, \delta \mathbf{u}) = \int_{\Omega_{em}} (\boldsymbol{\sigma} : \delta \boldsymbol{\varepsilon}) c \, d\Omega - \int_{\Omega_{em}} (\mathbf{b} \cdot \delta \mathbf{u}) c \, d\Omega - \int_{\Omega_{em}} (\mathbf{t} \cdot \delta \mathbf{u}) |\nabla c| \, d\Omega = 0 \quad (18)$$

If the boundary traction is formulated in terms of the boundary normal \mathbf{n} , for example a pressure load p , we can use (9) to re-write the surface integral as follows

$$\int_{\Omega_{em}} (p \mathbf{n} \cdot \delta \mathbf{u}) |\nabla c| \, d\Omega = \int_{\Omega_{em}} p \nabla c \cdot \delta \mathbf{u} \, d\Omega \quad (19)$$

Readers interested in a more details on convergence and accuracy of diffuse Neumann boundary conditions are referred to the computational study in the Appendix.

4.2. Dirichlet boundary conditions

In the next step, we consider the variational formulation (2) and (3), from which we obtain the symmetric Nitsche method [51, 52]. We assume again a suitable phase-field solution c whose diffuse interface represents the sharp Dirichlet boundary Γ_D . We then use the identities (5) and (6) to replace integrals over the physical domain Ω and its sharp boundary Γ_D by integrals over the embedding domain Ω_{em} . The result is the following geometrically diffuse formulation of Nitsche’s method:

Find the displacements \mathbf{u} such that $\delta W_{\mathcal{K}} = \delta W_{\mathcal{f}}$, where

$$\begin{aligned} \delta W_{\mathcal{K}}(\mathbf{u}, \delta \mathbf{u}) &= \int_{\Omega_{\text{em}}} (\boldsymbol{\sigma} : \delta \boldsymbol{\varepsilon}) c \, d\Omega \\ &\quad - \int_{\Omega_{\text{em}}} \mathbf{u} \cdot (\delta \boldsymbol{\sigma} \cdot \nabla c) \, d\Omega - \int_{\Omega_{\text{em}}} (\boldsymbol{\sigma} \cdot \nabla c) \cdot \delta \mathbf{u} \, d\Omega + \beta \int_{\Omega_{\text{em}}} \mathbf{u} \cdot \delta \mathbf{u} |\nabla c| \, d\Omega \end{aligned} \quad (20)$$

$$\delta W_{\mathcal{f}}(\delta \mathbf{u}) = \int_{\Omega_{\text{em}}} \mathbf{b} \cdot \delta \mathbf{u} \, d\Omega - \int_{\Omega_{\text{em}}} \hat{\mathbf{u}} \cdot (\delta \boldsymbol{\sigma} \cdot \nabla c) \, d\Omega + \beta \int_{\Omega_{\text{em}}} \hat{\mathbf{u}} \cdot \delta \mathbf{u} |\nabla c| \, d\Omega \quad (21)$$

The stabilization parameter β ensures coercivity of the bilinear form and hence stability of the finite element method. In analogy to Nitsche's method based on sharp interfaces, it is proportional to the elastic material parameter and a configuration-dependent constant, and inversely proportional to a suitable mesh size. In the scope of this work, we empirically choose β as 5 times Young's modulus. This choice resulted in stable finite element computations in all simulations, while an influence of the stabilization term on the convergence behavior could not be observed in the numerical tests. For more information on accuracy, convergence and stabilization, interested readers are referred to the computational study in the Appendix and further results reported in [61] that focuses on the diffuse Nitsche method from a numerical analysis viewpoint. In particular, the latter provides a generalization of the eigenvalue based estimation of the stabilization parameter and a comparison with consistent penalty-type methods derived for example in [27].

4.3. Imaging data vs. phase-fields: the link back to the voxel finite cell method

Although the convergence of the diffuse method exhibits significant differences to the accuracy of the finite cell method with sharply defined domains, there is a sweet spot when diffuse boundaries are combined with the voxel finite cell method. Our idea is based on the following rationale:

1. Combining the voxel finite cell method for the evaluation of the volume integrals and the diffuse interface method for the evaluation of the surface integrals leads to a method that does not require any explicit representation of geometric entities.
2. The geometric fidelity of the voxel finite cell method, and hence the maximum accuracy level of its physical solution fields, is limited by the available resolution of the imaging data. The limiting parameter is the maximum voxel spacing Δ .
3. The accuracy of the diffuse method is limited through the length scale ε that governs the width of the diffuse boundary region. Consequently, the voxel finite cell method and the diffuse boundary method exhibit the same limitation in terms of accuracy and convergence.

This indicates that, if the two limiting factors Δ and ε are properly related, the combination of the voxel finite cell method with the diffuse boundary strategy enables the same accuracy as the voxel finite cell method with sharply defined surfaces, but removes the roadblock of explicit surface parametrization.

To consolidate this idea, we will first summarize the corresponding changes in the variational form. The core component of the voxel finite cell method described in Section 2.3 is to use quadrature rules based on voxel data for numerically integrating volume integrals. In view of our target application in image-based bone strength analysis, we assume that we have approximations of Ω based on one or several phase-field functions c and a rasterized voxel representation Ω_{vox} . Since both approximations are defined over the complete embedding domain Ω_{em} , we can replace phase-field volume integrals by voxel integrals as follows

$$\int_{\Omega_{\text{em}}} Q c \, d\Omega \approx \int_{\Omega_{\text{vox}}} Q \, d\Omega \quad (22)$$

We now apply (22) to all volume terms in the diffuse boundary methods introduced in (18) through (21). Merging all terms leads to the following single variational formulation: Find the displacement

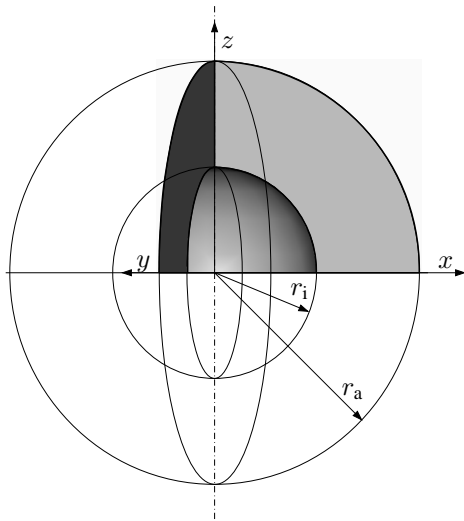


Figure 9. A thick spherical shell.

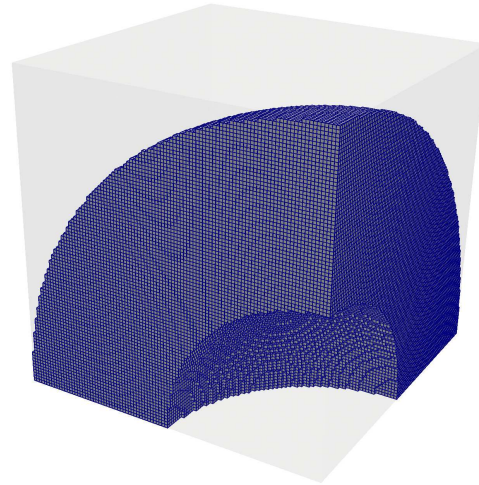


Figure 10. Voxel model (resolution $\Delta = 1$).

field \mathbf{u} such that $\delta W_{\mathbf{K}} = \delta W_f$, where

$$\begin{aligned} \delta W_{\mathbf{K}}(\mathbf{u}, \delta \mathbf{u}) &= \int_{\Omega_{\text{vox}}} \boldsymbol{\sigma} : \delta \boldsymbol{\varepsilon} \, d\Omega \\ &\quad - \int_{\Omega_{\text{em}}} \mathbf{u} \cdot (\delta \boldsymbol{\sigma} \cdot \nabla c_D) \, d\Omega - \int_{\Omega_{\text{em}}} (\boldsymbol{\sigma} \cdot \nabla c_D) \cdot \delta \mathbf{u} \, d\Omega + \beta \int_{\Omega_{\text{em}}} \mathbf{u} \cdot \delta \mathbf{u} \, |\nabla c_D| \, d\Omega \end{aligned} \quad (23)$$

$$\begin{aligned} \delta W_f(\delta \mathbf{u}) &= \int_{\Omega_{\text{vox}}} \mathbf{b} \cdot \delta \mathbf{u} \, d\Omega + \int_{\Omega_{\text{em}}} (\mathbf{t} \cdot \delta \mathbf{u}) \, |\nabla c_N| \, d\Omega \\ &\quad - \int_{\Omega_{\text{em}}} \hat{\mathbf{u}} \cdot (\delta \boldsymbol{\sigma} \cdot \nabla c_D) \, d\Omega + \beta \int_{\Omega_{\text{em}}} \hat{\mathbf{u}} \cdot \delta \mathbf{u} \, |\nabla c_D| \, d\Omega \end{aligned} \quad (24)$$

We note that (23) and (24) require further assumptions. First, we have split the phase-field c into two individual phase-fields c_N and c_D whose diffuse boundary regions approximate the sharp Neumann and Dirichlet boundaries. Second, in the multi-dimensional case, we assume that each component of the traction vector \mathbf{t} and the given displacement vector $\hat{\mathbf{u}}$, initially defined as functions on the sharp surfaces Γ_N and Γ_D , can be extended along the surface normal such that they are well-defined over the complete diffuse interface region [27].

4.4. 3D benchmark: a spherical thick shell

To illustrate accuracy and convergence of the voxel finite cell method with phase-field boundary conditions, we consider the spherical thick shell shown in Fig. 9. We assume an inner radius $R_i = 50$, an outer radius $R_a = 100$, Young's modulus $E = 10,000$, Poisson ratio $\nu = 0.3$, and either an internal pressure $p = 50$ as a Neumann condition or the equivalent boundary displacement $u_r = 0.2$ in radial direction as a Dirichlet condition. Due to symmetry, we consider only one eighth of the original problem. There exists an analytical solution [62, 63] in spherical coordinates $\{r, \phi, \theta\}$ that yields the exact strain energy $U_{ex} = 157,079.6326794896$.

For the geometric description of its volume, we consider either the sharp boundary representation shown in Fig. 9 or a corresponding voxel model of the embedding cube with an isotropic voxel resolution of $\Delta = 1$. The latter is illustrated in Fig. 10 that plots all voxels with Young's modulus $E = 10,000$, omitting all voxels with no stiffness outside the thick shell. For the geometric description of the inner surface, where Neumann or Dirichlet boundary conditions need to be applied, we consider either a sharp surface given by a very fine tessellation or the gradient of a

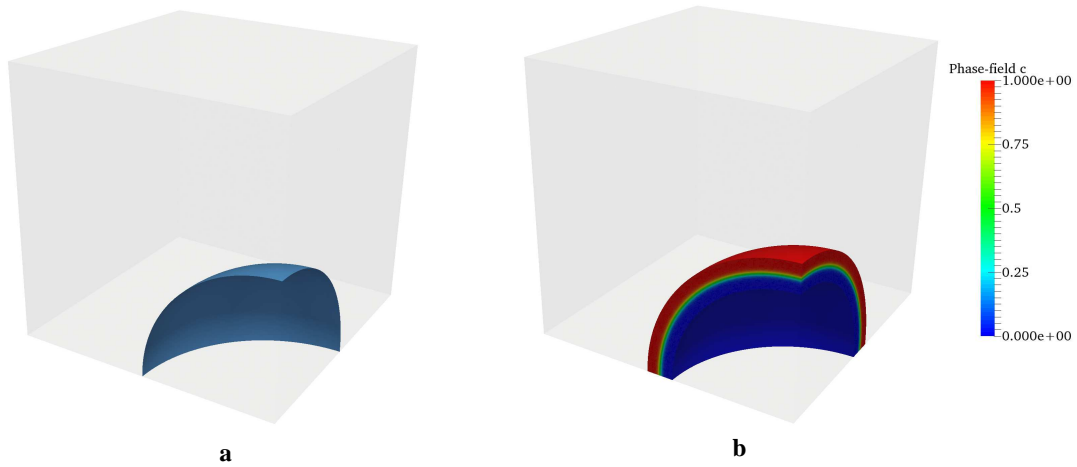


Figure 11. Geometric description of the inner surface: (a) sharp (very fine tessellation), (b) diffuse (phase-field with resolution $\varepsilon = 1$).

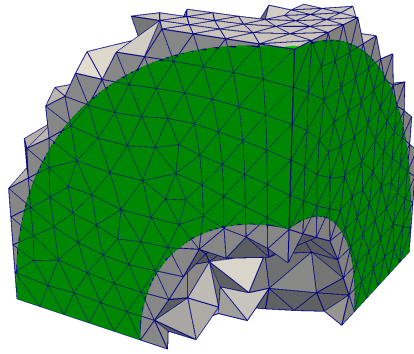


Figure 12. Initial unfitted finite element mesh employed in all voxel finite cell computations. All elements away from the physical domain (shaded in green) have been removed.

diffuse phase-field function, generated analytically as

$$c(r) = \frac{1}{2} \left(1 + \tanh \left(\frac{r - R_i}{\varepsilon} \right) \right) \quad (25)$$

Figure 11 illustrates both surface representations. We observe that both the voxel model and the diffuse phase-field model are characterized by a characteristic length scale, the voxel spacing Δ and the phase-field parameter ε , respectively. We note that if the voxel model is known, we can generate a corresponding phase-field representation via the Allen-Cahn problem as described in Section 3.2. If the phase-field function is known, we can generate a corresponding voxel representation by assigning full stiffness to all elements of a given voxel grid, where the phase-field is larger than 0.5 in its center.

In the first step, we employ the tetrahedral finite cell method, where integration over the volume is based on the sharp representation and integration over surfaces is based either on the sharp explicit or the diffuse implicit surface representations shown in Figs. 11a and 11b, respectively. To capture the volumetric geometry in cut elements, we employ the recursive quadrature scheme summarized in Section 2.2. We use quadratic tetrahedral meshes generated for the embedding cube, where all elements are removed, for which the phase-field stays below 10^{-6} in the element support. Symmetry boundary conditions along straight boundaries are imposed strongly. Figure 12 illustrates the initial unfitted mesh.

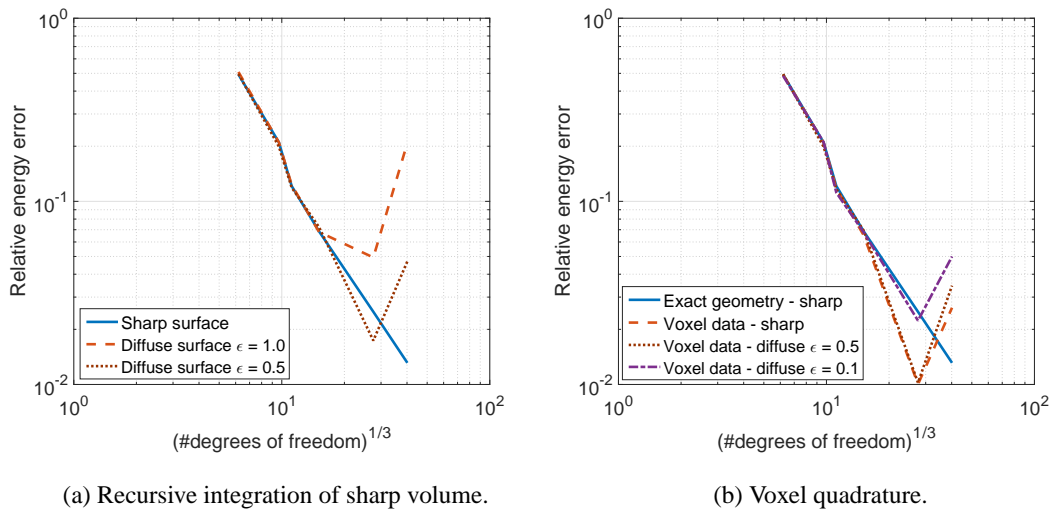


Figure 13. Neumann boundary conditions at inner spherical boundary for the spherical thick shell problem: Convergence in strain energy for sharp and diffuse surface integration.

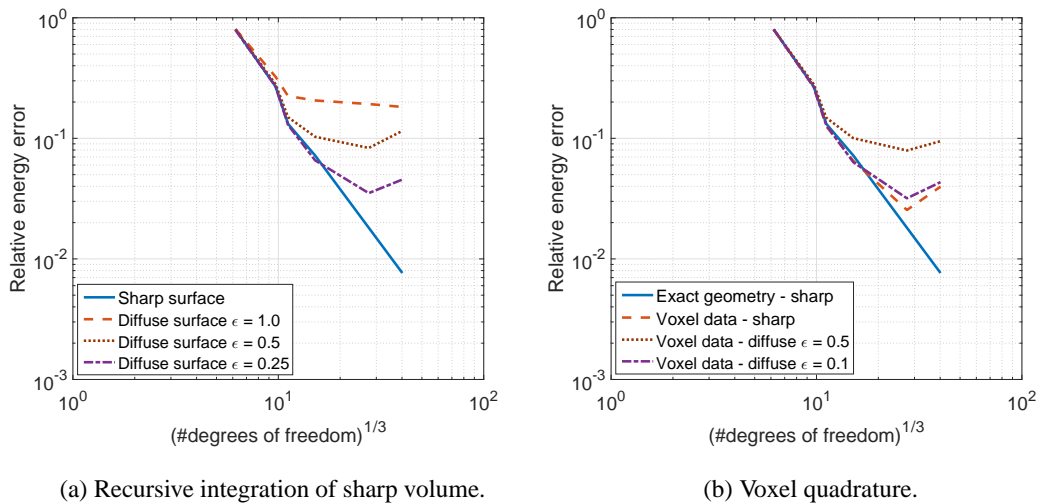


Figure 14. Dirichlet boundary conditions at inner spherical boundary for the spherical thick shell problem: Convergence in strain energy for sharp and diffuse surface integration.

We examine the effect of diffuse boundary conditions on the accuracy of the finite cell method by measuring the strain energy error defined over the sharp volume. Figures 13a and 14a plot the relative error under mesh refinement for Neumann and Dirichlet boundary conditions at the inner surface, respectively. We observe that the boundary conditions based on a sharp surface enable optimal convergence rates throughout the complete accuracy range. Diffuse boundary conditions based on the phase-field function (25) enable optimal convergence rates in the pre-asymptotic range, but level off at a critical error level that is controlled by the characteristic length scale parameter ϵ . These results confirm the convergence behavior outlined above for the one-dimensional bar.

In the second step, we repeat the same study, but employ the voxel finite cell method. The underlying voxel model Ω_{vox} that implicitly describes the volume of the thick spherical shell is shown in Fig. 10. To capture the volumetric geometry, we employ the voxel quadrature scheme of Section 2.3. Figures 13b and 14b plot the corresponding relative error in strain energy for

the Neumann and Dirichlet case, respectively. In addition, the sharp surface results are added as a reference. We observe that convergence curves level off at a critical accuracy level, even if Neumann and Dirichlet boundary conditions are imposed at a sharply defined surface. These results confirm that the accuracy of the voxel finite cell method is limited by the voxel resolution. Of particular interest from an engineering point of view is the pre-asymptotic range, where sharp and diffuse boundary conditions achieve exactly the same accuracy and optimal rates of convergence. These results support our initial hypothesis that the voxel finite cell method with diffuse boundary conditions enables the same accuracy as the voxel finite cell method with sharply defined surfaces.

4.5. Relating phase-field length scale, voxel spacing, and mesh size

The numerical behavior of the benchmark tests demonstrate that the success of the voxel finite cell method with diffuse boundary conditions depends on a suitable relation between the length scales involved in the method. These are the characteristic length scale of the phase-field solution, ε , that controls the width of the diffuse boundary region, the spacing of the voxels, Δ , that controls the resolution of the voxel model, and the mesh size, h , that controls the accuracy of the finite element approximation of the solution fields.

We observe in Figs. 13b and 14b that if we properly relate the two length scale parameters Δ and ε , the convergence curves obtained for diffuse boundary conditions level off at approximately the same critical accuracy level. According to the numerical tests, $\varepsilon = 0.5\Delta$ seems a good choice. Figures 13 and 14 also show that the strain energy error increases again when the mesh size has passed the critical point, where the convergence curve levels off from the reference. Our observations indicate that the reason for this phenomenon are spurious stress oscillations in the diffuse boundary regions. They start to appear when the mesh size is small enough to resolve the solution fields in the part of the diffuse region outside of the voxel model that has no stiffness (see also Fig. 15). From a practical viewpoint, it is therefore important to bound the minimum mesh size h in terms of ε . Our numerical tests indicate that for quadratic basis functions, $h > 10\varepsilon$ is a reliable lower bound for the mesh size that ensures that stress oscillations do not occur. Therefore, we can summarize the relation between the three inherent length scales as follows

$$h \gtrsim 10\varepsilon \approx 5\Delta \quad (26)$$

We note that the constraint on the mesh size h by the voxel spacing Δ in (26) that automatically follows from the above considerations is in line with the limitation that the accuracy of the voxel finite cell method cannot be increased by mesh refinement beyond the voxel resolution [15, 17].

4.6. Implementation aspects

The accuracy of diffuse boundary conditions relies on accurately integrating the phase-field gradient throughout the complete diffuse boundary region. This requires an adequate number of quadrature points in the diffuse boundary region. Standard element quadrature rules are not sufficient, since in general the length scale parameter ε is significantly smaller than the element size h . In the context of the finite cell method, we can leverage recursive subdivision quadrature as described in Section 2.2 to achieve accurate integration of the phase-field gradient. The application of recursive quadrature in the diffuse boundary region is illustrated in Fig 15. Our numerical tests indicate that a sub-cell size of 2ε is sufficient to achieve full accuracy.

Combining the voxel finite cell method with diffuse boundary conditions leads to several pitfalls that require special care. On the one hand, the part of the diffuse interface region not covered by the voxel model still needs to be integrated, even if there is no stiffness. In the context of the finite cell method, we suggest the following strategy: We only remove those elements from the discretization of the embedding domain that have no support in the voxel volume and for which the phase-field stays below a tolerance (in our case $c < 10^{-6}$) everywhere in the element support. To maintain solvability of the system, we assign a very small stiffness (in our case $c < 10^{-8}$) to all voxels outside the physical domain, which is in line with the original concept of the finite cell method [29, 30]. Figure 15 illustrates this strategy.

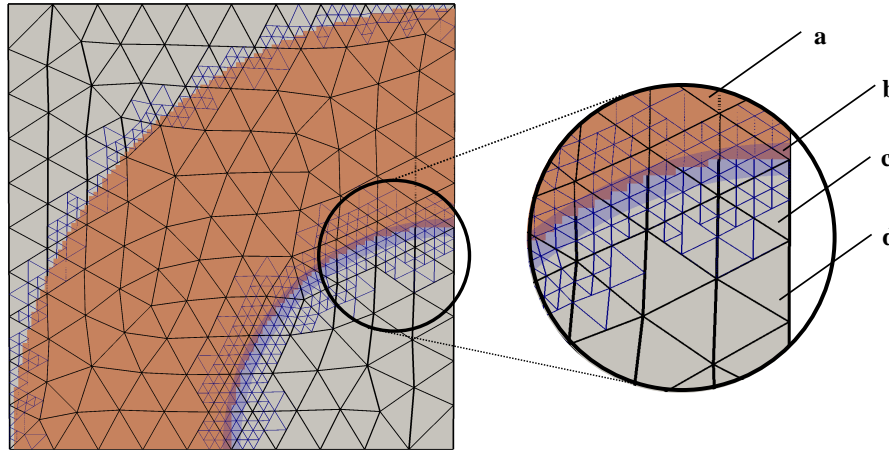


Figure 15. (a) Voxel data, (b) diffuse boundary band, (c) element outside the physical domain but cut by the diffuse band, therefore not removed, (d) element completely outside the physical domain, will be removed. For elements as in (c), all quadrature points will be assigned a small stiffness to maintain solvability of the system.

On the other hand, the evaluation of the surface terms of the diffuse Nitsche method in (23) and (24) cannot rely on the volumetric voxel model for choosing the appropriate stiffness parameters. We recall that the derivation of the formulation of diffuse boundary conditions assumes that all surface input is extended in normal direction. Therefore, when evaluating the surface terms of the diffuse Nitsche method outside of the voxel model, we still need to assume full stiffness for those terms. In our implementation, we trace the voxels along the negative normal vector (9) until we find a voxel with significant stiffness.

5. PATIENT-SPECIFIC BONE STRENGTH ANALYSIS WITHOUT EXPLICIT GEOMETRY RECONSTRUCTION

In the following, we demonstrate the validity, accuracy and effectiveness of the voxel finite cell method with diffuse phase-field boundary conditions for the patient-specific strength analysis of bones. We focus on vertebra and femur bones that are of particular interest for patient-specific strength prediction, e.g., due to the critical role they play in osteoporosis-induced fractures.

5.1. Femur

We first consider a femur that constitutes a well-studied test case, for which results from a number of previous successful computational and experimental studies are available. These studies were performed in the groups of ERNST RANK at the Technische Universität München, Germany, and ZOHAR YOSIBASH at the Ben-Gurion University of the Negev, Beer-Sheva, Israel, and have led to a number of publications, e.g., [15, 16, 22, 23, 24]. The input for the femur simulations are quantitative CT scans in the form of a DICOM[†] file that provides the HU for a specific layer and pixel spacing. It was obtained by a clinical Philips Brilliance 64 CT (Eindhoven, The Netherlands): 120kVp, 250mAs, 1.25 slice thickness 0.195mm (bone shaft tilted by 5° with respect to the axial direction of the CT scan). A calibration phantom provides a linear conversion between HU and an equivalent mineral density $\rho_{eqm}[g/cm^3]$ that is then transferred to voxel-wise Young's moduli.

[†]Digital Imaging and Communications in Medicine

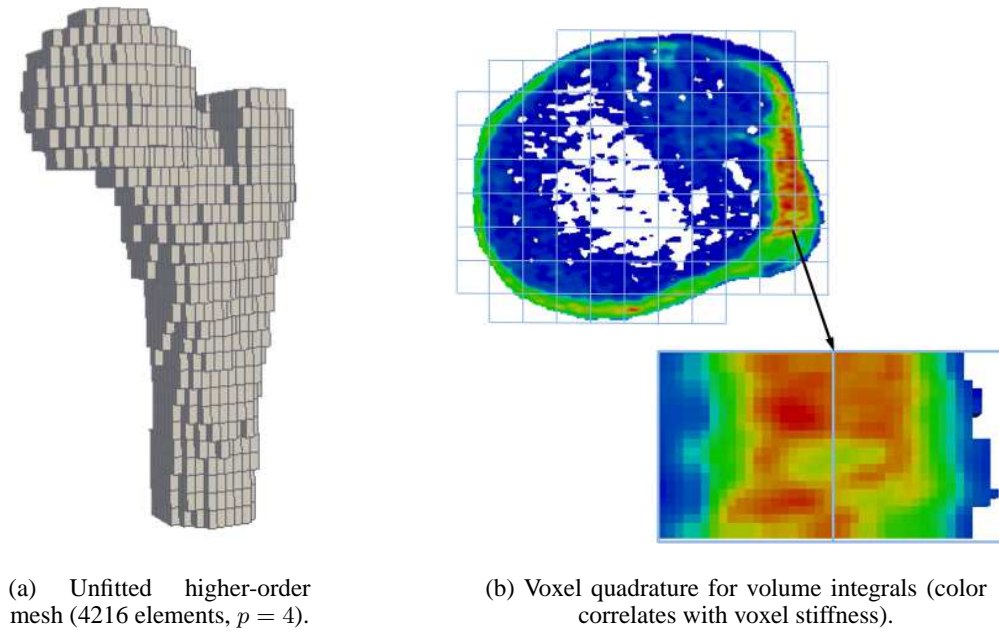


Figure 16. Femur: Discretization with the voxel finite cell method.

5.1.1. Discretization with the voxel finite cell method. Using an unfitted mesh, we discretize the embedding domain with 4216 hexahedral finite elements of polynomial degree $p = 4$, where each hexahedral element exactly covers $(15 \times 15 \times 5)$ voxels. Elements outside the physical domain are removed from the discretization. For the evaluation of the volumetric integrals, we adopt the voxel quadrature rules that have been described in Section 2.3. We assume an isotropic heterogeneous linear elastic material and determine the Young's modulus at each voxel with the following model relations

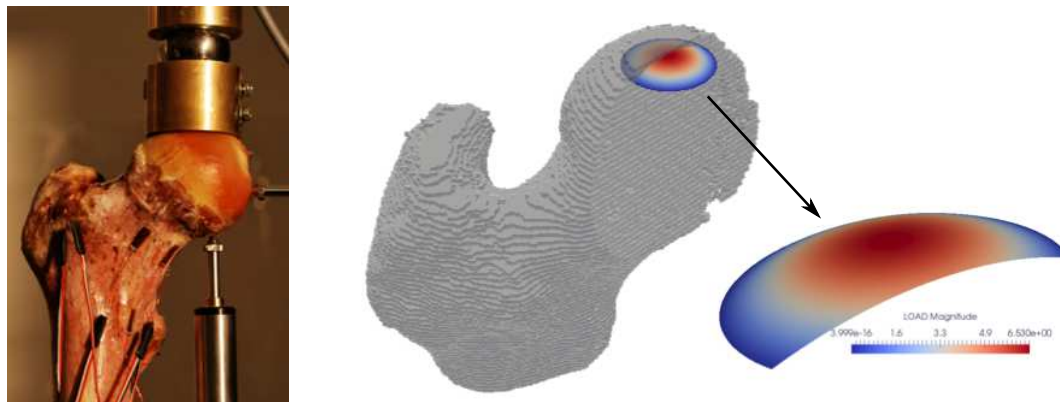
$$\rho_{ash} = (1.22 \rho_{eqm} + 0.0523) [g/cm^3] \quad (27)$$

$$E_{trab} = 5307 \times \rho_{ash} + 469 [MPa], \quad \text{if } 0 < \rho_{ash} < 0.4 \quad (28)$$

$$E_{cort} = 10200 \times \rho_{ash}^{2.01} [MPa], \quad \text{if } \rho_{ash} \geq 0.4 \quad (29)$$

where ρ_{ash} denotes the ash density corresponding to ρ_{eqm} [19]. In addition, we use a homogeneous Poisson's ratio $\nu = 0.3$. The distal face of the femur is a flat plane, where displacement boundary conditions can be easily applied with the sharp Nitsche method. Figure 16 illustrates the discretization of the femur in the context of the voxel finite cell method, including the distribution of HU and voxel quadrature.

5.1.2. Loading on sharp explicit surfaces. In line with the experimental set-up shown in Fig. 17a, we need to apply a load of 1,000 N on the femoral head. Following previous successful computational studies [22, 23, 15], the compression zone is idealized as a spherical cap, over which a parabolically distributed load is defined (see Fig. 17b). The corresponding Neumann boundary condition in the voxel finite cell method is taken into account by tessellating the spherical cap and evaluating surface integrals via standard quadrature rules in each triangular facet [30, 47]. However, the accurate imposition of the loading via a sharply defined surface requires to find a location that guarantees a tight fit with the thin cortical shell of the femoral head. In particular, if some part of the loading cap is located above the cortical shell, where the stiffness is below the stiffness threshold, the loading cannot be properly transferred into the structure, leading to a significant loss of accuracy. Therefore, the entire loading surface must be covered by voxels that contain non-zero stiffness.



(a) Load configuration.

(b) Sharp cap surface and load magnitude distribution.

Figure 17. Loading via a sharply defined explicit surface on the femoral head.

Figure 18 illustrates the difficulty of tightly fitting a sharp surface to the thin cortical shell. As a consequence, the resulting simulation workflow critically relies on manual intervention.

5.1.3. Loading on diffuse implicit phase-fields. To remove the bottleneck of finding an explicitly defined loading surface, we establish a workflow that employs the voxel finite cell method and the diffuse formulation of Neumann boundary conditions based on a suitable phase-field. Its individual steps are illustrated in Fig. 19. To obtain a diffuse representation of the loading surface, we first identify a suitable mesh, on which we can solve the Allen-Cahn problem. To minimize the computational effort, we suggest to use a sphere whose position and circumference at the intersection with the cortical shell corresponds to the cylindrical loading device in the experiment (see Fig. 17a). The sphere can be easily generated from the experimental set-up. We note that one could also use an extended cylinder, if finding a sphere is too cumbersome. We then determine a suitable initial condition for the Allen-Cahn problem from the imaging data that is located within the sphere. Based on the initial condition, we generate a cloud of local h -values, from which we can generate an adaptive tetrahedral mesh (see [17] for details on octree-based adaptive mesh generation). We use standard linear tetrahedral elements, where the smallest element size corresponds to the length-scale parameter ε of the Allen-Cahn equation, which in turn is chosen

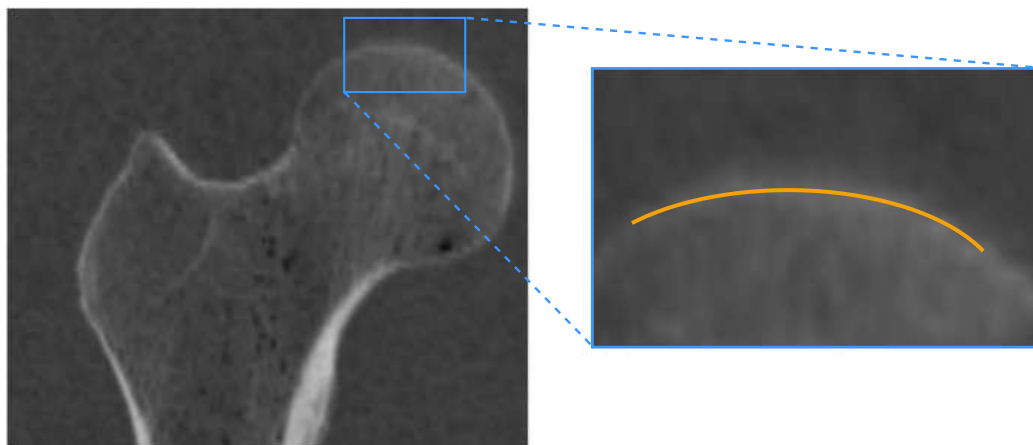


Figure 18. The thin cortical shell makes it difficult to find a cap position that guarantees a tight fit.

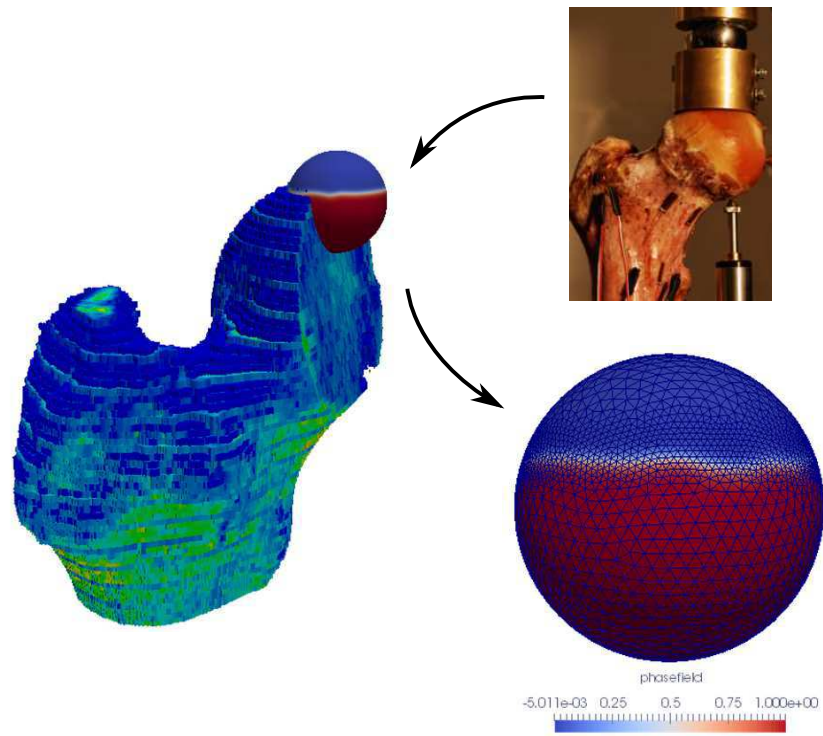


Figure 19. Workflow for imposing loads on the femoral head in a diffuse sense.

as one half of the largest voxel spacing ($\varepsilon = 0.5\Delta$). Solving the Allen-Cahn problem as detailed in Section 3.3, we finally obtain a phase-field function that is shown in Fig. 19.

Using the phase-field, we can impose the corresponding Neumann boundary condition in a diffuse sense by computing the traction term in (24). As shown in Fig. 17a, the traction vector \mathbf{t} is assumed to be a parabolic function that depends on the distance from the center of the cap. Since we know the position of the center of the cylindrical loading device, we can easily compute the distance of each point and determine a relative traction intensity. The direction of the traction vector \mathbf{t} is known and does not depend on the geometric description of the loading surface. Since we do not know the total area of the diffuse implicit surface in advance, we cannot directly control the total load that is imposed. We therefore scale the entries of the right hand side vector of the discrete system in such a way that the absolute value of the load resultant corresponds to 1,000 N.

The workflow outlined in Fig. 19 involves several steps and requires an additional computational cost compared to imposing loads on a sharp surface. However, it eliminates the need for the construction of a tightly fitted spherical cap, while each of the associated steps can be potentially automated. The result is a diffuse phase-field that is guaranteed to tightly fit the cortical shell surface. Therefore, the resulting modification of the voxel finite cell method is able to directly operate on imaging data, completely avoiding a transfer of implicit voxel-based bone geometry into explicit volume and surface parametrizations.

5.1.4. Validation and comparison. We assess the accuracy of the diffuse formulation by comparing numerical strain results with experimental measurements available for three different shaft inclination angles (0° , 7° , 15°). In the experiments conducted in ZOHAR YOSIBASH's group at the Ben-Gurion University, Beer Sheva, Israel, the largest principal strains, e.g., either ε_1 (tension) or ε_3 (compression), were measured at 11 different locations. We note that these measurements have been successfully used in several other validation studies [22, 23, 24]. Figure 20 illustrates the locations and the numbering of the strain results. We compute corresponding strains with the voxel finite cell method, using either the sharply defined load cap or the diffuse phase-field representation

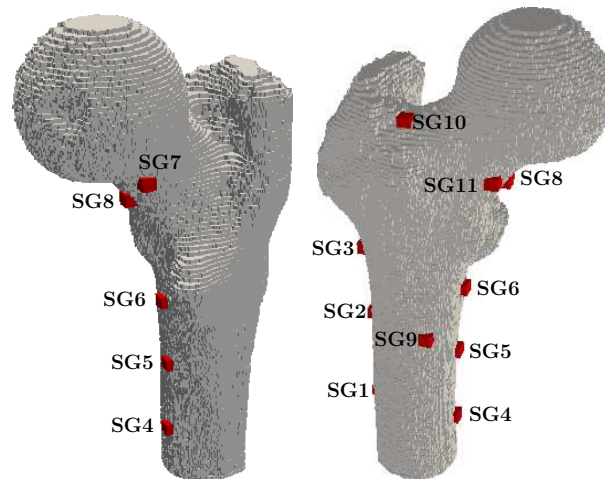


Figure 20. Position and numbering of the 11 strain gauges on the surface of the femur specimen.

of the load surface described above. We note that all simulations are based on the same unfitted finite element mesh shown in Fig. 16a. Numerical strains from the simulation results were extracted at the 11 locations on the bone's surface by averaging 15 values taken in the direct vicinity of the strain gauge location. A more detailed description of the data acquisition from the simulation results and the corresponding assumptions are given in [15].

Figure 21 provides three plots (one for each inclination angle of the shaft) that compare the relative error of both sets of simulation results with respect to the experimental reference value for each of the 11 locations. We observe that the voxel finite cell method with both loading surface representations is able to correctly predict the strain behavior of the femur bone. For each gauge location at each inclination angle, the relative error obtained with the diffuse boundary conditions is in the same order of magnitude (or better) as the one obtained with the sharply defined loading surface. In addition, the simulation results obtained with the diffuse phase-field consistently correlate with the simulation results obtained with the sharp cap. Considering the complete set of results, we observe that the relative error in the diffuse case tends to be slightly higher than in the sharp case. However, only two out of 33 data points show a sizable increase at a significant error level. These are gauge 8 at an inclination angle of 0° with 21% error (diffuse) vs. 8% error (sharp) and gauge 10 at an inclination angle of 7° with 53% error (diffuse) vs. 22% error (sharp).

Figure 22 provides linear regression plots of the experimental measurements versus the two sets of simulation results. We observe that the voxel finite cell method with both loading surface representations achieves an excellent overall correlation between experiments and numerical predictions, with coefficients of determination R^2 that are consistently above 0.85 ($R^2=1$: fully correlated, optimum; $R^2=0$: fully uncorrelated). To put these correlation values into perspective, we compare them to values that have been reported for similar studies in the literature. For example, good correlations between numerically predicted and experimental results can be found in [64] based on standard finite element analyses with conforming meshes ($R^2 > 0.89$), and in [65] based on a meshless MCM approach ($R^2 > 0.85$). The present validation study therefore demonstrates the validity and accuracy of the phase-field based boundary conditions in the context of the voxel finite cell method.

5.2. Vertebra

In the second example, we apply the diffuse phase-field formulation to impose traction and displacement constraints on the surface of a vertebra. Due to their complicated geometry, creating an explicit parametrization of the loading and support surfaces at the upper and lower faces of the vertebra constitutes a significant challenge for the automation of simulation workflows. This

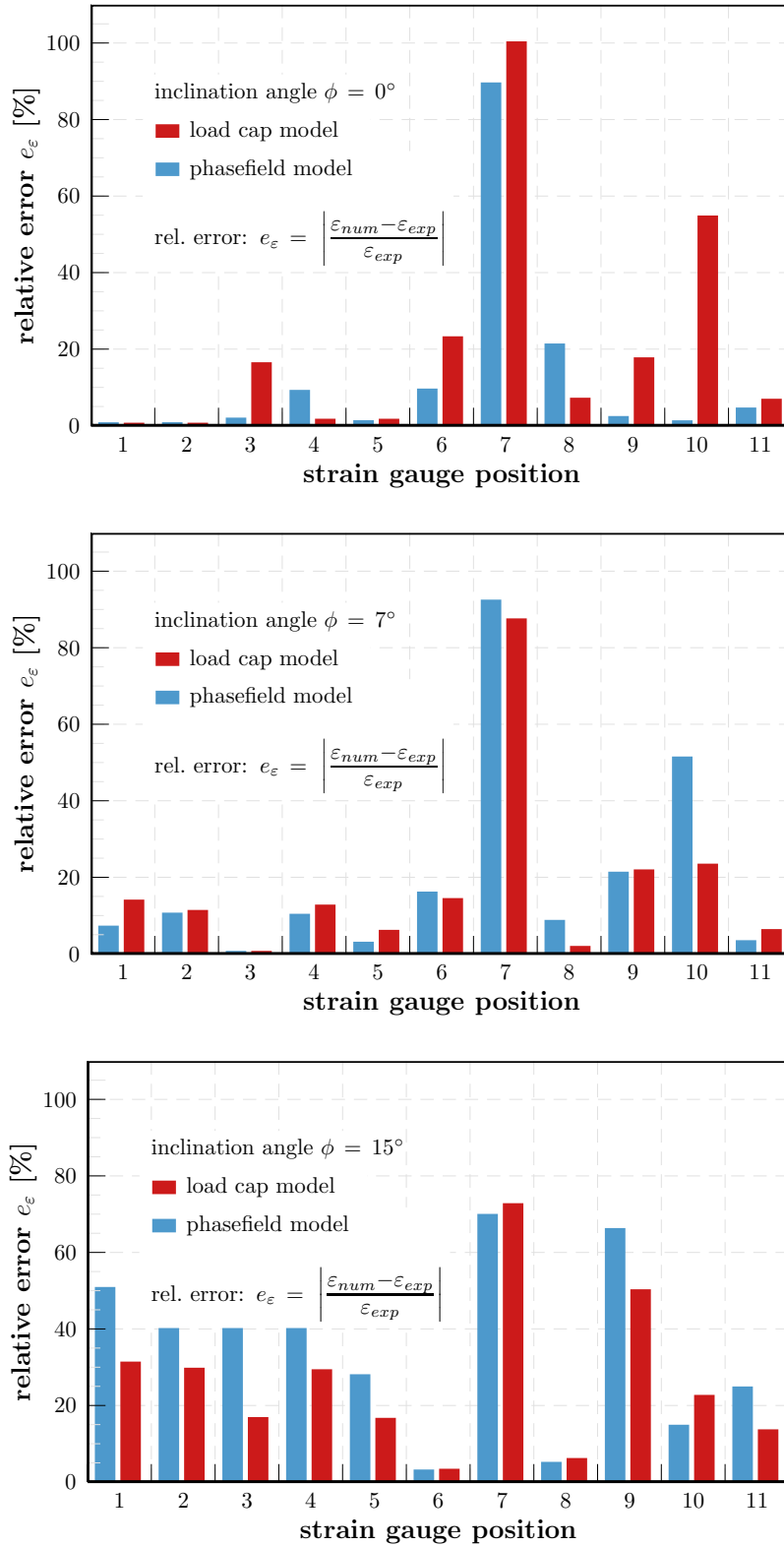


Figure 21. Comparison of relative errors in strain for three different inclinations of the shaft (experiment vs. simulations based on a sharp loading cap and a diffuse phase-field surface).

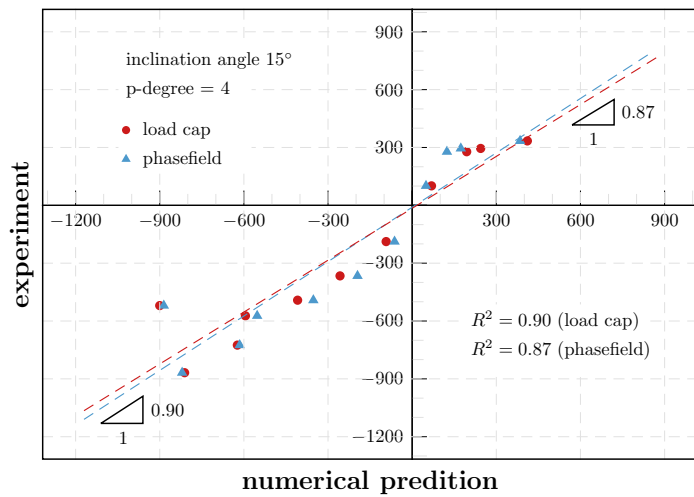
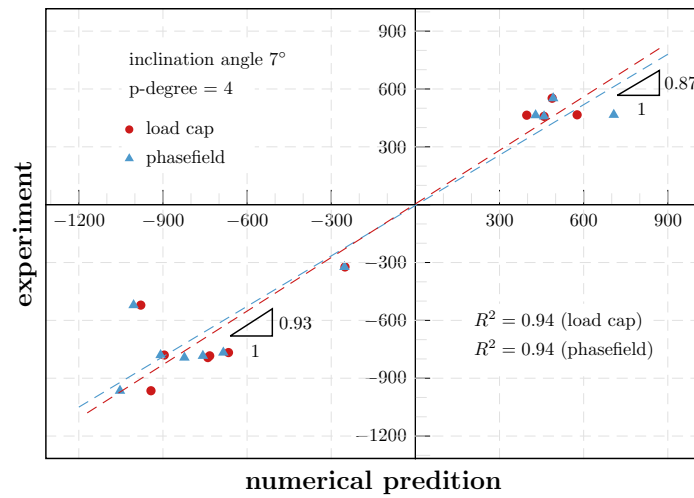
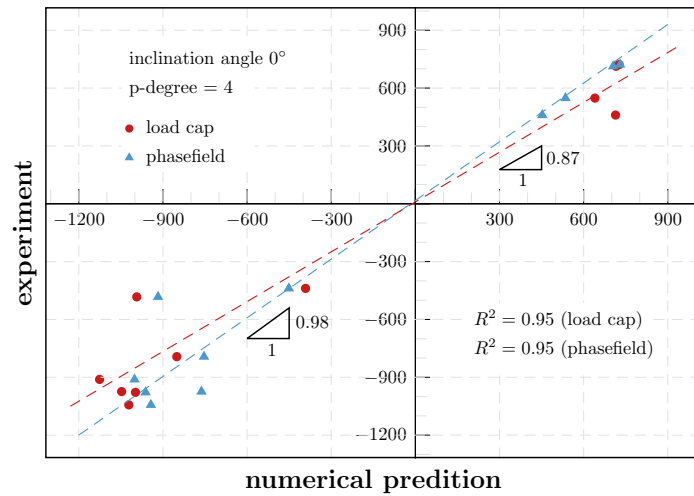


Figure 22. Linear regression of strains for three different inclinations of the shaft (experiment vs. simulations based on a sharp loading cap and a diffuse phase-field surface).

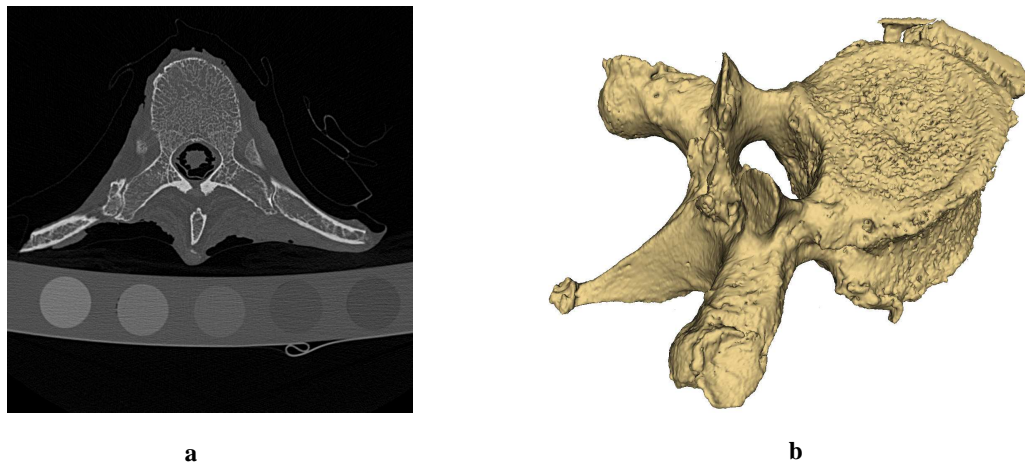


Figure 23. Vertebra: (a) layer of the original CT scan, (b) voxel model of the geometry of the segmented vertebra

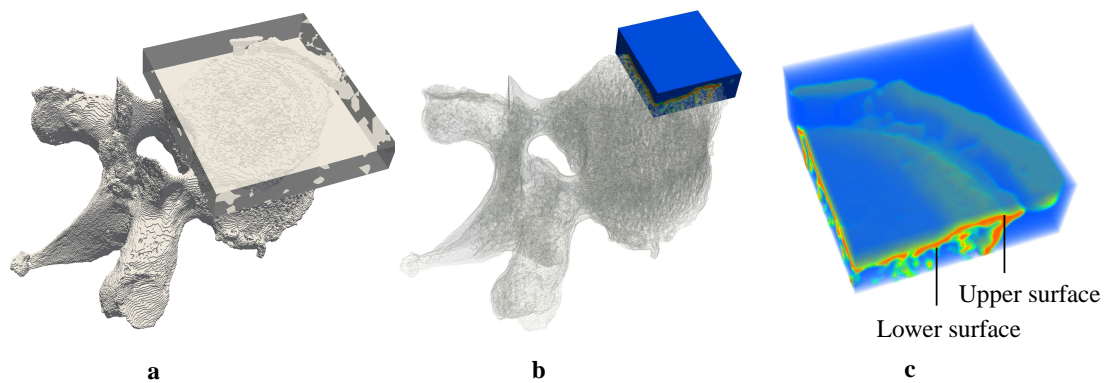


Figure 24. Diffuse representation of the upper surface: (a) domain for computing the Allen-Cahn problem, (b) and (c) part of the phase-field solution

example therefore illustrates the advantages and flexibility of our approach for imposing boundary conditions at very complex surfaces.

5.2.1. Imaging data and material properties. The geometric basis of the structure is again an implicit voxel model that has been derived from CT scans as illustrated in Fig. 23. CT images were acquired on a iCT (Philips Healthcare, Best, Netherlands) using a high spatial resolution kernel (YB). CT intensity values were converted to bone mineral density values using a dedicated calibration phantom (Mindways, CA, USA). We note that we separated the vertebra from the surrounding bone structures with the help of the open-source medical image processing library ITK[‡]. The voxel spacing is $\Delta_x = \Delta_y = 0.1465\text{mm}$ and $\Delta_z = 0.3\text{mm}$. For each voxel in the vertebra structure, we assume the following material parameters: Young's modulus $E = 10\text{GPa}$, Poisson's ratio $\nu = 0.3$ [66].

5.2.2. Diffuse phase-field representations of upper and lower faces. To minimize computational cost, we define the Allen-Cahn equation on an embedding rectangular domain that contains only the boundary region instead of the complete vertebral body. This is illustrated in Fig. 24a for the upper face of the vertebral body. We choose the length scale of the phase-field as $\epsilon = 0.15\text{mm}$, one

[‡]Insight Segmentation and Registration Toolkit (ITK), <https://itk.org/>

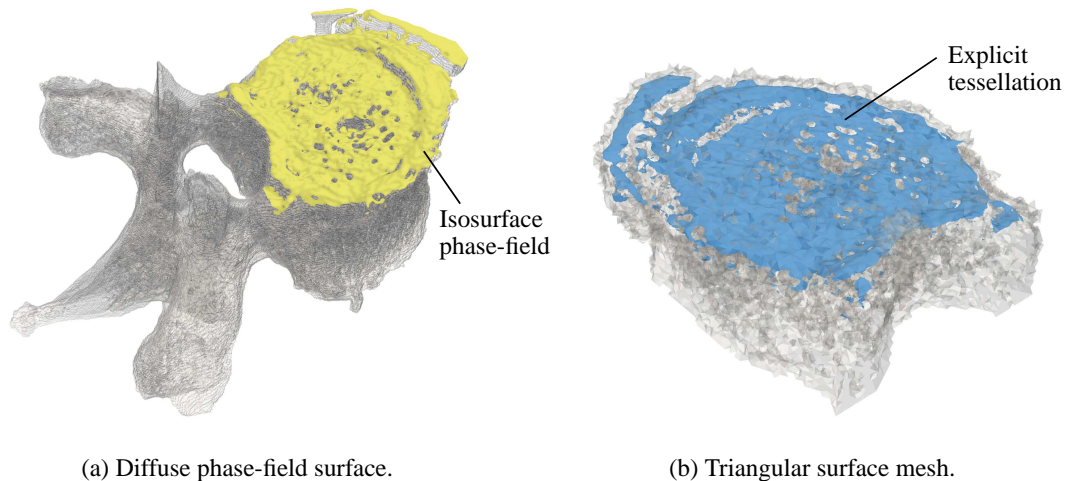


Figure 25. Implicit and explicit description of the upper vertebra surface.

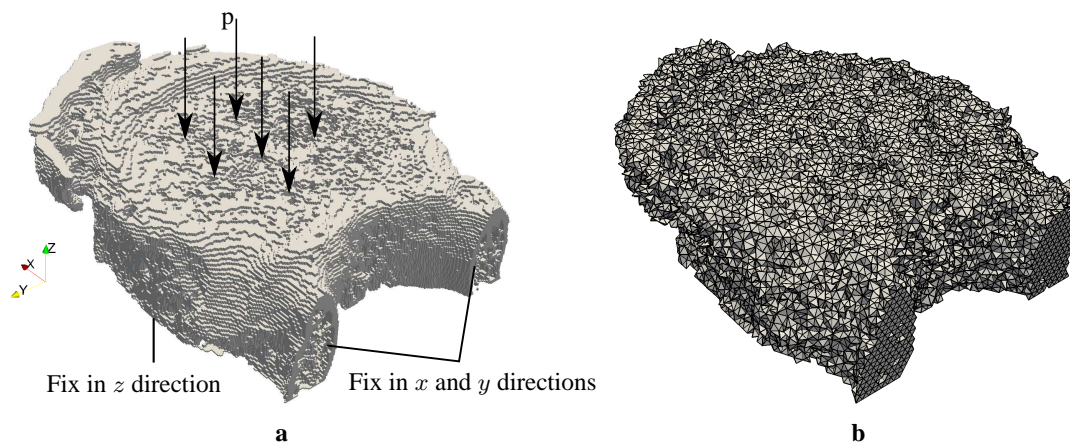


Figure 26. Upper half of the vertebral body: (a) Voxel model and boundary conditions, (b) unfitted tetrahedral mesh.

half of the largest voxel spacing $\Delta_z = 0.3\text{mm}$, and discretize the rectangular domain with linear tetrahedral elements of mesh size $h = 0.1\text{mm}$. Figure 24b and 24c illustrate the resulting phase-field representation of the upper surface of the vertebra. In particular, we can observe in Fig. 24c that the phase-field resolves both the upper and lower side of the cortical shell. To distinguish between the upper and the lower side, we monitor the normal vector of the diffuse surface, defined in (9). If at any point in the phase-field domain the normal vector points away from the vertebra core, we assume that this point belongs to the surface, where diffuse boundary conditions are to be imposed. To be able to compare accuracy with the voxel finite cell method and a sharp boundary, we also manufacture a corresponding explicit surface representation by transferring the phase-field isosurface at $c = 0.5$ into a tessellation composed of approx. 13,000 triangular facets. The corresponding outward surfaces of the vertebra are shown in Figs. 25a and 25b, respectively.

5.2.3. Analysis of the upper half of the vertebra. Since we are particularly interested in the strength of the vertebral body that carries the bulk of the load, we cut away the vertebral arch from the body. In a first step, we consider only the upper half of the vertebra shown in Fig. 26a. We discretize the structure with a quadratic tetrahedral finite element mesh shown in Fig. 26b. The unfitted mesh consists of 252,558 nodes and 757,674 degrees of freedom. In the sense of the voxel finite cell

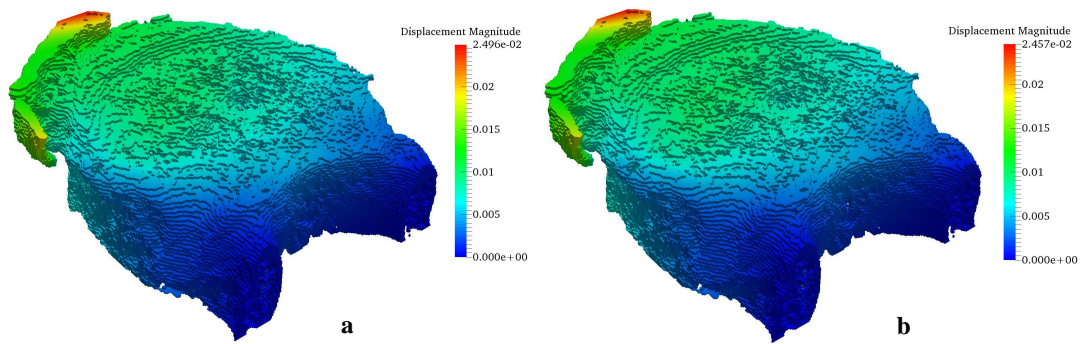


Figure 27. Displacement solution obtained with the voxel finite cell method: (a) diffuse Neumann boundary conditions on implicit phase-field surface, (b) Neumann boundary conditions on sharply defined upper surface

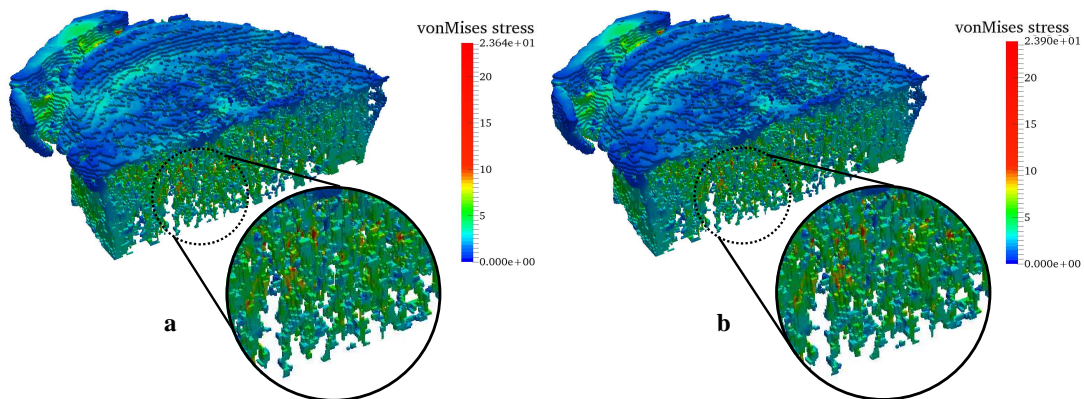


Figure 28. von Mises stress for the upper half of vertebra: (a) diffuse phase-field boundary conditions, (b) boundary conditions on sharply defined tessellation.

method, we apply voxel quadrature with one subdivision level of sub-cells, so that quadrature points can better resolve the geometric details of the voxel model. We assume a distributed compressive load $p = 1N/mm^2$ at the top surface that we can impose either in a diffuse sense via the phase-field solution or in a sharp boundary sense via the tessellation. To distinguish between the upper and the lower side of the fully resolved cortical shell (see Fig. 24c), we monitor again the normal vector of the diffuse surface (9) at each quadrature point. We add the Gauss point contribution of the diffuse loading term to the load vector, only if the vertical component of the normal vector is within the range $n_z \geq 0.8$. This constitutes an effective way to prevent that loads are taken into account for portions of the diffuse phase-field representation that correspond to surfaces at the lower side of the cortical shell and to horizontal surfaces at the lateral sides of the vertebra. Displacement boundary conditions are imposed at the planar mesh boundaries at the cutting planes as outlined in Fig. 26a.

Figure 27 plots the total displacements obtained with the voxel finite cell method with diffuse and sharp imposition of the traction boundary condition at the top of the vertebral body. The corresponding von Mises stresses are plotted in Fig. 28, including zooms of part of the trabecular region. We observe that the displacement and stress solutions match very well. In particular, the zoom areas indicate that the stress pattern obtained with the diffuse and sharp variants agree very well both qualitatively and quantitatively.

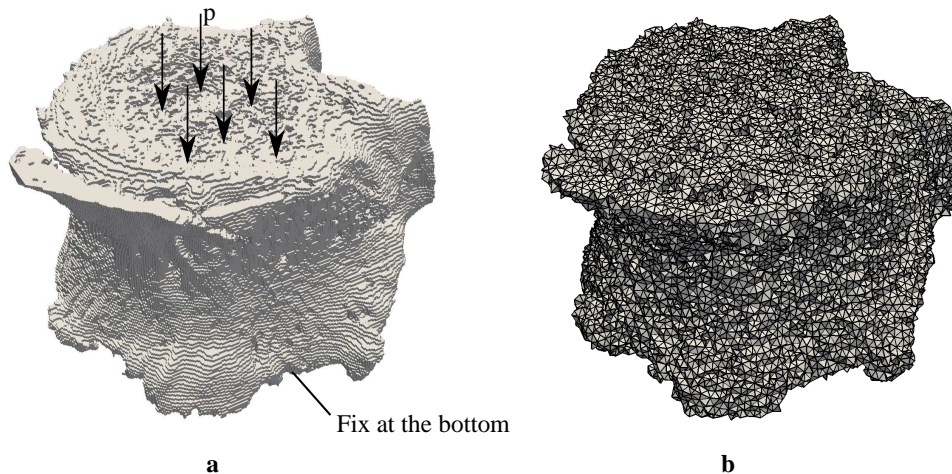


Figure 29. Full vertebra: (a) Voxel model and boundary conditions, (b) unfitted finite element mesh

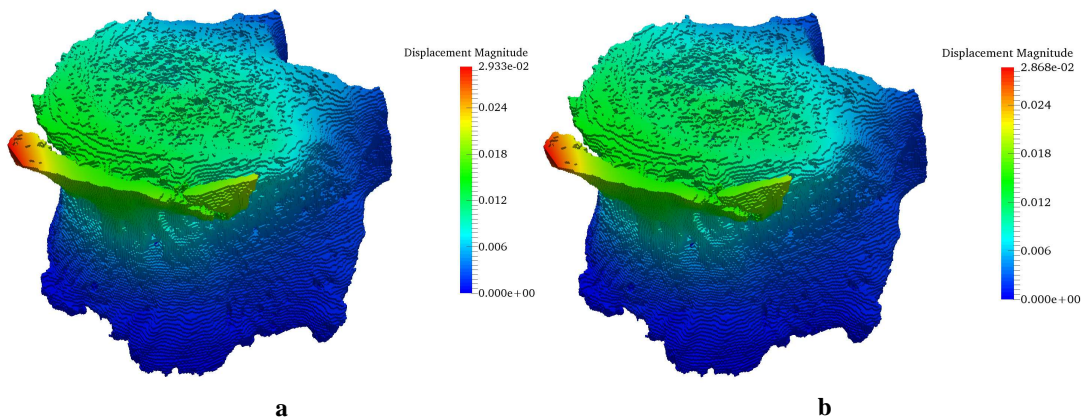


Figure 30. Displacement magnitude: (a) diffuse phase-field boundary conditions, including the diffuse Nitsche method (b) boundary conditions on sharply defined tessellations.

For a more rational comparison, we evaluate the relative difference between the diffuse and sharp boundary condition variants in the sense of a voxel version of the L^2 norm as follows

$$d_{L^2} = \sqrt{\frac{\sum_{vox} (a_{diff} - a_{sharp})^2}{\sum_{vox} (a_{sharp})^2}} \times 100\% \quad (30)$$

where a_{diff} and a_{sharp} denote either the total displacement or von Mises stress at each voxel in the vertebral body, computed with with diffuse and sharp boundary conditions, respectively. Following the definition (30), we obtain an L^2 difference of 1.96% for the total displacements and an L^2 difference of 3.36% for the von Mises stress. These results illustrate that the diffuse formulation of Neumann boundary conditions yields excellent accuracy.

5.2.4. Analysis of the full vertebral body. In a second step, we consider the full vertebral body shown in Fig. 29a. The full structure features complex surface geometries at the upper and lower side faces. We discretize the full structure with an unfitted quadratic tetrahedral mesh shown in Fig. 29b, which consists of 494,151 nodes and 1,482,453 degrees of freedom. We again define a compressive load of $p = 1N/mm^2$ on top, but also support the structure at the outward surface of the cortical shell at the bottom. We employ the voxel finite cell method with voxel quadrature as described in the previous paragraph, where we apply diffuse phase-field formulations of Neumann

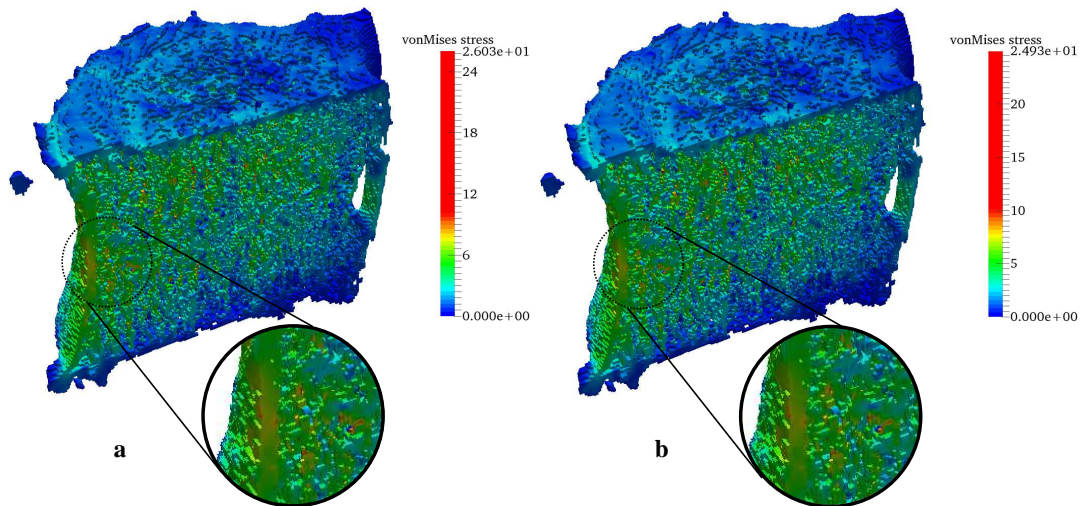


Figure 31. von Mises stress (a) diffuse phase-field boundary conditions, including the diffuse Nitsche method (b) boundary conditions on sharply defined tessellations.

and Dirichlet boundary conditions, including the diffuse Nitsche method. To this end, we compute a second phase-field representation for the lower boundary region of the vertebra in the same way as shown in Fig. 24 for the upper boundary region. We note that at the bottom surface, only quadrature points, for which the vertical component of the phase-field normal vector (9) lies within $n_z \leq -0.8$, are accounted for in the diffuse Nitsche method. For comparison, we manufacture a corresponding tessellation that explicitly parametrizes the lower surface by triangular facets.

Figures 30 and 31 plot the solution fields in terms of the total displacements and the von Mises stress, respectively, obtained with the voxel finite cell method and diffuse and sharp boundary conditions. We note that in the latter case, the displacement constraint at the bottom is imposed with the standard form of Nitsche's method on the sharp tessellation. We observe in Figs. 30 and 31 that both displacement and stress solutions match very well. We highlight again the zoom areas in the stress plots that show equivalent stress patterns and agree very well qualitatively and quantitatively. Following the definition 30, we compute relative L^2 differences between the diffuse and sharp variants, which results in a relative difference of 3.18% for the total displacement magnitude and a relative difference of 4.96% for the von Mises stress. These results confirm the excellent agreement of the two simulation variants, extending this statement to the diffuse Nitsche method.

6. SUMMARY AND CONCLUSIONS

The voxel finite cell method enables a seamless transfer of diagnostic imaging data into patient-specific bone discretizations, but still requires the explicit parametrization of boundary surfaces to impose traction and displacement boundary conditions. In this paper, we presented a phase-field formulation for imposing traction and displacement constraints in a diffuse sense, integrated in the context of the voxel finite cell method.

We started by briefly reviewing the building blocks of the voxel finite cell method, i.e., unfitted finite element meshes, the imposition of unfitted boundary conditions, and recursive subdivision and voxel quadrature rules. We then discussed a methodology for transferring imaging data into a corresponding phase-field function via solving an Allen-Cahn problem with imaging data as initial condition. We formulated a set of requirements that determine a valid phase-field function in terms of diffuse geometry modeling. These include: (a) the phase-field monotonically decreases from one to zero; (b) with decreasing length scale parameter, the phase-field converges to the Heaviside function; (c) given sufficient smoothness of the sharp boundary, the negative normalized gradient of

the phase-field converges to the sharp normal vector; (d) the spike of the phase-field gradient centers at the sharp boundary. We showed that the metastable short-term phase-field solution of the initial boundary value problem based on the Allen-Cahn equation satisfies all of these requirements.

We then introduced diffuse phase-field formulations for the imposition of Neumann and Dirichlet boundary conditions (i.e., loads and displacements). Following geometric arguments, we employed the approximation of the Dirac distribution based on the phase-field gradient to transfer surface integrals at the boundary into volumetric integrals. We argued that for consistency, the phase-field approximation of the Dirac distribution needs to replicate the property that its integration across the diffuse boundary region yields one. We applied this mechanism to the surface integrals of Neumann and Dirichlet boundary conditions. For the latter, we derived a diffuse variant of Nitsche's method with empirically estimated stabilization parameter. We illustrated for a benchmark test how different representations based on sharply defined geometry, diffuse phase-fields and imaging data affect accuracy and convergence behavior of the finite cell method.

On the one hand, our numerical tests illustrated that diffuse boundary methods lead to sub-optimal convergence, including a pronounced error in the diffuse boundary region. On the other hand, the voxel finite cell method with diffuse boundary conditions enables the same accuracy as the voxel finite cell method with sharply defined surfaces, if the characteristic length scale of the phase-field, ε , the voxel spacing of the imaging data and the mesh size of the finite element approximation are properly related. We found from our numerical tests that ε should be approximately one half the voxel size and that the mesh size must be larger than 10 times ε .

We illustrated the strength of the voxel finite cell method with diffuse phase-field boundary conditions for the patient-specific stress analysis of femur and vertebra bone structures, whose geometry and stiffness distribution are provided by CT scans. For the femur, we outlined a simplified workflow that eliminates the time-intensive manual identification of a sharp loading surface and its location within the thin cortical shell of the femoral head. Our simulation results demonstrated that diffuse boundary conditions lead to the same excellent overall correlation between experiments and numerical predictions as standard sharp boundary conditions. The numerical simulation of a compression test for different vertebra configurations illustrated that diffuse boundary conditions are able to handle extremely complicated surfaces. We demonstrated that simulations based on diffuse and sharp boundary conditions produce stress patterns that are indistinguishable from each other. The accuracy of diffuse boundary conditions were further confirmed by the relative difference in a L^2 voxel norm between diffuse and sharp results, which consistently led to differences as small as 5% or less for displacements and stresses in all vertebra configurations.

The combination of the voxel finite cell method with diffuse boundary conditions leads to a new methodology that is able to directly operate on imaging data, completely avoiding the transfer of implicit imaging data into explicit volume and surface parametrizations. At the same time, it reliably delivers the level of accuracy in predicting mechanical bone behavior that is required for clinically relevant applications. We therefore believe that the new methodology provides a potential pathway for further automating patient-specific simulation, with the eventual goal of establishing evidence-based predictive tools in clinical practice.

Acknowledgments. L.H. Nguyen, S.K.F. Stoter and D. Schillinger gratefully acknowledge support from the National Science Foundation (CISE-1565997). J.S. Kirschke received research grants from the European Research Council (ERC) under the European Union's Horizon 2020 research and innovation programme (grant agreement No. 637164 – ERC-2014-STG) and the German Research Foundation (BA 4085 2/1). The Minnesota Supercomputing Institute (MSI) of the University of Minnesota has provided computing resources that have contributed to the research results reported within this paper (<https://www.msi.umn.edu/>), which is also gratefully acknowledged.

APPENDIX

The appendix provides interested readers with a more detailed computational study that illustrates the convergence behavior of diffuse Neumann and Dirichlet boundary conditions.

A-1. Neumann boundary conditions

To illustrate accuracy and convergence of the phase-field formulation (18), we consider the example of a one-dimensional bar shown in Fig. 32. The bar is fixed at its left end and loaded by a sine-shaped load and a concentrated force F at its right end. To obtain a diffuse geometry for this example, we use the analytical solution of the one-dimensional Allen-Cahn equation (15), with the diffuse boundary position $a = 1.0$ located at the right end. For an illustration of the phase-field, we refer to Figs. 5 and 6 in Section 3. We discretize the variational form (18) with standard quadratic nodal elements, where we consider an embedding domain $\Omega_{em} = [0.0, 2.0]$ such that the displacement constraint at the left end $x = 0$ can be imposed strongly. To ensure that phase-field quantities are integrated accurately, we increase the number of Gauss points in elements in the diffuse boundary region. We remove elements from the discretization, for which the phase-field stays below 10^{-6} in the complete support.

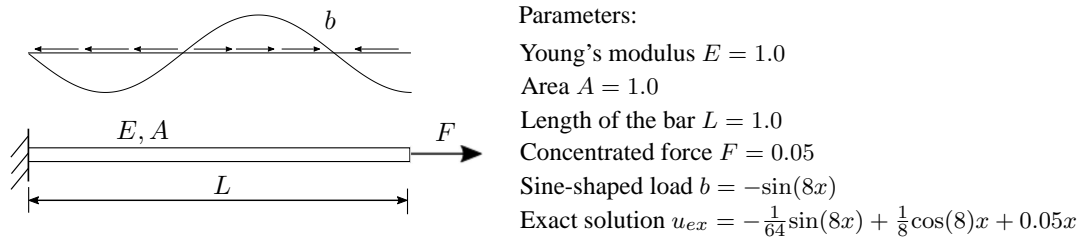


Figure 32. Uni-axial bar example.

Figure 33a plots the relative error in the H^1 semi-norm when the initial mesh is uniformly refined. We note that we compute the error with respect to the exact domain Ω . We observe that optimal rates of convergence are achieved, if both domain and surface are taken into account exactly in a sharp boundary sense. The corresponding convergence curve is hence adopted as a reference. The geometrically diffuse formulation (18) yields a suboptimal rate of convergence, even if we tie the characteristic length scale of the phase-field to the mesh size ($h = \varepsilon$). The reason is that the overall accuracy is controlled by the low-order accuracy of the phase-field, as the value of ε is bisected.

In view of the voxel finite cell method, where volumetric terms are integrated based on a voxel model, we integrate all volumetric terms exactly and only impose the concentrated load in a diffuse sense. Figure 33a plots the corresponding convergence behavior for three different values of ε that are now held constant during mesh refinement. We observe that in this case, the diffuse formulation is able to achieve the same accuracy as a sharp boundary method in the pre-asymptotic range. The convergence curve levels off when the geometry error of the diffuse boundary becomes larger than the approximation error and therefore starts to dominate the total error. The three curves plotted in Fig. 33a also demonstrate that the maximum accuracy directly correlates with the length scale parameter ε used in the diffuse phase-field representation.

Finally, we focus on the strains computed for $\varepsilon = 0.0025$. The first error curve plotted in Fig. 33b refers to the integration over the exact domain Ω and reproduces the corresponding convergence curve shown in Fig. 33a. We then compute the error over the bulk of the domain, but omit the diffuse boundary region. Figure 33b shows the error in H^1 semi-norm under mesh refinement for the domains $(L - 2.5\varepsilon)$ and $(L - 5\varepsilon)$. We observe that the solution in the bulk of the domain converges at optimal rates and the convergence curves approach the reference. This illustrates that the error due to a diffuse Neumann boundary condition accumulates in the diffuse boundary region.

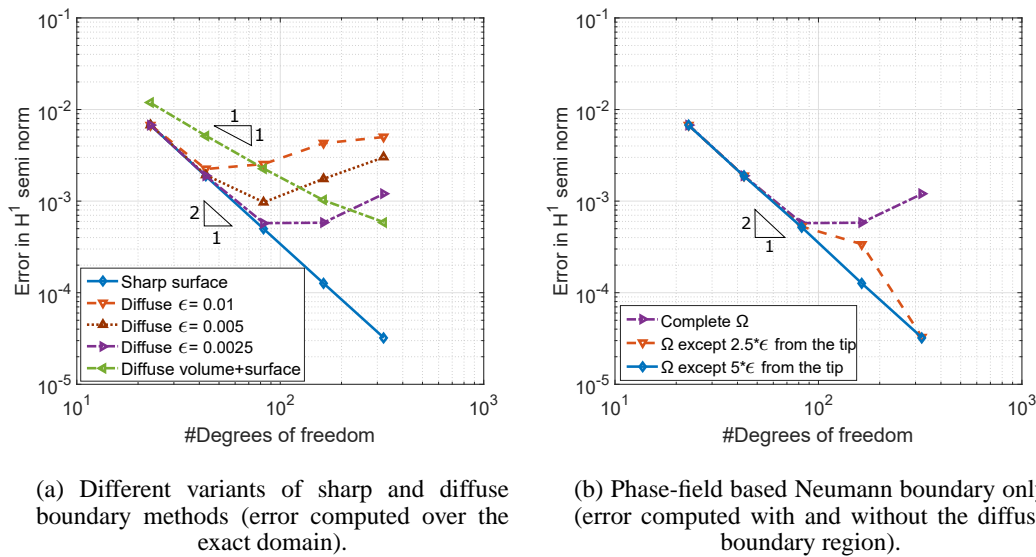


Figure 33. 1D bar with Neumann boundary condition: Convergence of the error in H^1 semi-norm.

A-2. Dirichlet boundary conditions

To briefly illustrate the performance of the diffuse Nitsche method, we modify the one-dimensional bar example by replacing the concentrated force F by a displacement constraint at the right end. The adjusted system along with the new exact solution is shown in Fig. 34. We use the same analytical phase-field function as above, so that we can strongly impose the displacement constraint at the left end, but use the diffuse Nitsche formulation (20) and (21) with $\hat{u} = 0$ at the right end. Figure 35a illustrates the convergence behavior of different variants of diffuse and sharp boundary methods obtained with the same quadratic finite element discretizations as above. The standard symmetric Nitsche approach with sharply defined domain and boundaries is again adopted as a reference. When tying the characteristic length scale of the phase-field to the mesh size ($h = \epsilon$), the geometrically diffuse formulation (18) yields suboptimal rates of convergence. We observe that the rate of convergence in the H^1 semi-norm assumes $\mathcal{O}(\epsilon)$ in the pre-asymptotic range, while in the asymptotic range, it tends towards $\mathcal{O}(\epsilon^{\frac{1}{2}})$. The same convergence behavior has been recently observed in similar methods, e.g., the consistent penalty-type diffuse interface method examined in [67] and corresponding convergence rates have been rigorously proved.

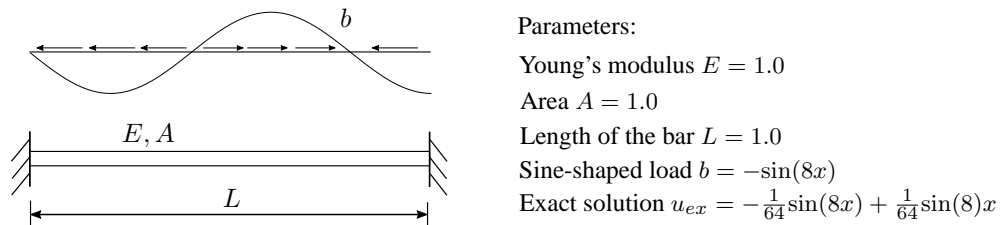
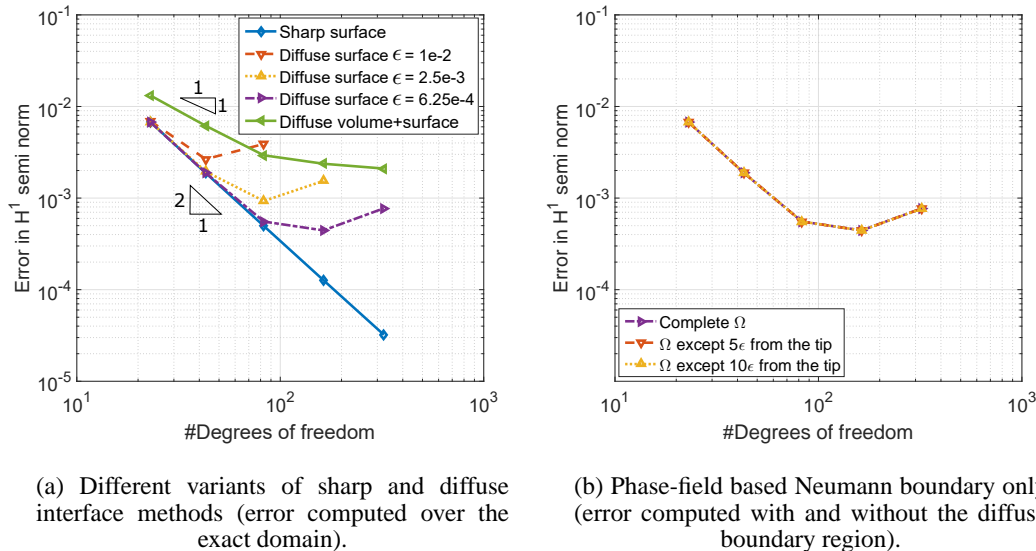


Figure 34. Uni-axial bar example with Dirichlet constraint.

In view of the voxel finite cell method, we test the numerical behavior for the case, when we integrate all volumetric terms exactly and only impose the Dirichlet constraint in a diffuse sense. Figure 35a plots the corresponding convergence behavior for three different values of ϵ that are now held constant during mesh refinement. The results confirm that in analogy to the Neumann case above, the diffuse Nitsche method is able to achieve the same optimal accuracy as a sharp boundary

method in the pre-asymptotic range. When the geometry error due to the diffuse boundary region becomes larger than the approximation error, the convergence curve levels off. Figure 35b compares the error in H^1 semi-norm under mesh refinement computed for the full domain L and for the domains $(L - 5\epsilon)$ and $(L - 10\epsilon)$ without the diffuse boundary region. We observe that all curves remain identical, indicating that the error due to a diffuse Dirichlet condition does not accumulate in the diffuse boundary region, but affects the complete domain.



(a) Different variants of sharp and diffuse interface methods (error computed over the exact domain).

(b) Phase-field based Neumann boundary only (error computed with and without the diffuse boundary region).

Figure 35. 1D bar with Dirichlet boundary condition: Convergence of the error in H^1 semi-norm.

REFERENCES

1. P.K. Zysset, E. Dall'Ara, P. Varga, and D.H. Pahr. Finite element analysis for prediction of bone strength. *BoneKey reports*, 2:386, 2013.
2. D.D. Cody, G.J. Gross, F.J. Hou, H.J. Spencer, S.A. Goldstein, and D.P. Fyhrie. Femoral strength is better predicted by finite element models than QCT and DXA. *Journal of Biomechanics*, 32(10):1013–1020, 1999.
3. R.P. Crawford, C.E. Cann, and T.M. Keaveny. Finite element models predict in vitro vertebral body compressive strength better than quantitative computed tomography. *Bone*, 33(4):744–750, 2003.
4. C. Graeff, F. Marin, H. Petto, O. Kayser, A. Reisinger, J. Peña, P. Zysset, and C.-C. Glüer. High resolution quantitative computed tomography-based assessment of trabecular microstructure and strength estimates by finite-element analysis of the spine, but not DXA, reflects vertebral fracture status in men with glucocorticoid-induced osteoporosis. *Bone*, 52(2):568–577, 2013.
5. M. Viceconti, R. Lattanzi, B. Antonietti, S. Paderni, R. Olmi, A. Sudanese, and A. Toni. CT-based surgical planning software improves the accuracy of total hip replacement preoperative planning. *Medical Engineering & Physics*, 25(5):371–377, 2003.
6. S.J. Shefelbine, P. Augat, L. Claes, and U. Simon. Trabecular bone fracture healing simulation with finite element analysis and fuzzy logic. *Journal of Biomechanics*, 38(12):2440–2450, 2005.
7. J.H. Keyak, S.A. Rossi, K.A. Jones, and H.B. Skinner. Prediction of femoral fracture load using automated finite element modeling. *Journal of Biomechanics*, 31(2):125–133, 1997.
8. M. Lengsfeld, J. Schmitt, P. Alter, J. Kaminsky, and R. Leppik. Comparison of geometry-based and CT voxel-based finite element modelling and experimental validation. *Medical Engineering & Physics*, 20(7):515–522, 1998.
9. M. Viceconti, M. Davinelli, F. Taddei, and A. Cappello. Automatic generation of accurate subject-specific bone finite element models to be used in clinical studies. *Journal of Biomechanics*, 37(10):1597–1605, 2004.
10. E. Schileo, F. Taddei, A. Malandrino, L. Cristofolini, and M. Viceconti. Subject-specific finite element models can accurately predict strain levels in long bones. *Journal of Biomechanics*, 40(13):2982–2989, 2007.
11. R. Carretta, S. Lorenzetti, and R. Müller. Towards patient-specific material modeling of trabecular bone post-yield behavior. *International Journal for Numerical Methods in Biomedical Engineering*, 29(2):250–272, 2013.
12. R. Hambli. Micro-CT finite element model and experimental validation of trabecular bone damage and fracture. *Bone*, 56(2):363–374, 2013.
13. Z. Yang, M. Ruess, S. Kollmannsberger, A. Düster, and E. Rank. An efficient integration technique for the voxel-based finite cell method. *International Journal for Numerical Methods in Engineering*, 91:457–471, 2012.

14. Z. Yang, S. Kollmannsberger, A. Düster, M. Ruess, E.G. Garcia, E. Burgkart, and E. Rank. Non-standard bone simulation: Interactive numerical analysis by computational steering. *Computing and Visualization in Science*, 14:207–216, 2012.
15. M. Ruess, D. Tal, N. Trabelsi, Z. Yosibash, and E. Rank. The finite cell method for bone simulations: Verification and validation. *Biomechanics and Modeling in Mechanobiology*, 11(3):425–437, 2012.
16. H. Wille, M. Ruess, E. Rank, and Z. Yosibash. Uncertainty quantification for personalized analyses of human proximal femurs. *Journal of Biomechanics*, 49(4):520–527, 2016.
17. V. Varduhn, M.-C. Hsu, M. Ruess, and D. Schillinger. The tetrahedral finite cell method: Higher-order immersogeometric analysis on adaptive non-boundary-fitted meshes. *International Journal for Numerical Methods in Engineering*, 107:1054–1079, 2016.
18. A. Stavrev, L.H. Nguyen, R. Shen, V. Varduhn, M. Behr, S. Elgeti, and D. Schillinger. Geometrically accurate, efficient, and flexible quadrature techniques for the tetrahedral finite cell method. *Computer Methods in Applied Mechanics and Engineering*, 2016.
19. J.H. Keyak and Y. Falkinstein. Comparison of in situ and in vitro CT scan-based finite element model predictions of proximal femoral fracture load. *Medical Engineering & Physics*, 25(9):781–787, 2003.
20. R. Blanchard, C. Morin, A. Malandrino, A. Vella, Z. Sant, and C. Hellmich. Patient-specific fracture risk assessment of vertebrae: A multiscale approach coupling X-ray physics and continuum micromechanics. *International Journal for Numerical Methods in Biomedical Engineering*, doi:10.1002/cnm.2760, 2016.
21. A. Düster, H.-G. Sehlhorst, and E. Rank. Numerical homogenization of heterogeneous and cellular materials utilizing the finite cell method. *Computational Mechanics*, 50:413–431, 2012.
22. Z. Yosibash, R. Padan, L. Joskowicz, and C. Milgrom. A CT-based high-order finite element analysis of the human proximal femur compared to in-vitro experiments. *ASME Journal of Biomechanical Engineering*, 129:297, 2007.
23. Z. Yosibash, N. Trabelsi, and C. Milgrom. Reliable simulations of the human proximal femur by high-order finite element analysis validated by experimental observations. *Journal of Biomechanics*, 40(16):3688–3699, 2007.
24. N. Trabelsi, Z. Yosibash, and C. Milgrom. Validation of subject-specific automated p-FE analysis of the proximal femur. *Journal of Biomechanics*, 42(3):234–241, 2009.
25. A. Bueno-Orovio, V.M. Pérez-García, and F.H. Fenton. Spectral methods for partial differential equations in irregular domains: the spectral smoothed boundary method. *SIAM Journal on Scientific Computing*, 28(3):886–900, 2006.
26. A. Rätz and A. Voigt. PDE's on surfaces—a diffuse interface approach. *Communications in Mathematical Sciences*, 4(3):575–590, 2006.
27. X. Li, J. Lowengrub, A. Rätz, and A. Voigt. Solving PDEs in complex geometries: a diffuse domain approach. *Communications in Mathematical Sciences*, 7(1):81, 2009.
28. K.Y. Lervåg and J. Lowengrub. Analysis of the diffuse-domain method for solving PDEs in complex geometries. *arXiv preprint arXiv:1407.7480*, 2014.
29. J. Parvizian, A. Düster, and E. Rank. Finite cell method: h - and p - extension for embedded domain methods in solid mechanics. *Computational Mechanics*, 41:122–133, 2007.
30. A. Düster, J. Parvizian, Z. Yang, and E. Rank. The finite cell method for three-dimensional problems of solid mechanics. *Computer Methods in Applied Mechanics and Engineering*, 197:3768–3782, 2008.
31. E. Rank and H. Werner. An adaptive finite element approach for the free surface seepage problem. *International Journal for Numerical Methods in Engineering*, 23(7):1217–1228, 1986.
32. E. Rank and U. Weinert. A simulation system for diffusive oxidation of silicon: a two-dimensional finite element approach. *IEEE Transactions on Computer-Aided Design of Integrated Circuits and Systems*, 9(5):543–550, 1990.
33. K.E. Teigen, X. Li, J. Lowengrub, F. Wang, and A. Voigt. A diffuse-interface approach for modeling transport, diffusion and adsorption/desorption of material quantities on a deformable interface. *Communications in Mathematical Sciences*, 4(7):1009, 2009.
34. C.M. Elliott, B. Stinner, V. Styles, and R. Welford. Numerical computation of advection and diffusion on evolving diffuse interfaces. *IMA Journal of Numerical Analysis*, 31(3):786–812, 2011.
35. S. Aland, J. Lowengrub, and A. Voigt. Two-phase flow in complex geometries: A diffuse domain approach. *Computer Modeling in Engineering & Sciences*, 57(1):77, 2010.
36. K.E. Teigen, P. Song, J. Lowengrub, and A. Voigt. A diffuse-interface method for two-phase flows with soluble surfactants. *Journal of Computational Physics*, 230(2):375–393, 2011.
37. C. Miehe, M. Hofacker, and F. Welschinger. A phase field model for rate-independent crack propagation: Robust algorithmic implementation based on operator splits. *Computer Methods in Applied Mechanics and Engineering*, 199(45):2765–2778, 2010.
38. M.J. Borden, C.V. Verhoosel, M.A. Scott, Hughes T.J.R., and C.M. Landis. A phase-field description of dynamic brittle fracture. *Computer Methods in Applied Mechanics and Engineering*, 217–220:77–95, 2012.
39. D. Schillinger, M.J. Borden, and H.K. Stolarski. Isogeometric collocation for phase-field fracture models. *Computer Methods in Applied Mechanics and Engineering*, 284:583–610, 2015.
40. A. Mikelic, M.F. Wheeler, and T. Wick. A phase-field method for propagating fluid-filled fractures coupled to a surrounding porous medium. *SIAM Multiscale Modeling & Simulation*, 13(1):367–398, 2015.
41. G. Vilanova, I. Colominas, and H. Gomez. Capillary networks in tumor angiogenesis: From discrete endothelial cells to phase-field averaged descriptions via isogeometric analysis. *International Journal for Numerical Methods in Biomedical Engineering*, 29(10):1015–1037, 2013.
42. H. Gomez, L. Cueto-Felgueroso, and R. Juanes. Three-dimensional simulation of unstable gravity-driven infiltration of water into a porous medium. *Journal of Computational Physics*, 238:217–239, 2013.
43. D. Anders, C. Hesch, and K. Weinberg. Computational modeling of phase separation and coarsening in solder alloys. *International Journal of Solids and Structures*, 49(13):1557–1572, 2012.
44. J. Liu, C.M. Landis, H. Gomez, and T.J.R. Hughes. Liquid-vapor phase transition: Thermomechanical theory, entropy stable numerical formulation, and boiling simulations. *Computer Methods in Applied Mechanics and Engineering*, 297:476–553, 2015.

45. Y. Zhao, P. Stein, and B.-X. Xu. Isogeometric analysis of mechanically coupled Cahn-Hilliard phase segregation in hyperelastic electrodes of Li-ion batteries. *Computer Methods in Applied Mechanics and Engineering*, 297:325–347, 2015.
46. F. Xu, D. Schillinger, D. Kamensky, V. Varduhn, C. Wang, and M.-C. Hsu. The tetrahedral finite cell method for fluids: Immersogeometric analysis of turbulent flow around complex geometries. *Computers & Fluids*, doi:10.1016/j.compfluid.2015.08.027, 2016.
47. D. Schillinger and M. Ruess. The Finite Cell Method: A review in the context of higher-order structural analysis of CAD and image-based geometric models. *Archives of Computational Methods in Engineering*, 22(3):391–455, 2015.
48. D. Schillinger, M. Ruess, N. Zander, Y. Bazilevs, A. Düster, and E. Rank. Small and large deformation analysis with the p - and B-spline versions of the Finite Cell Method. *Computational Mechanics*, 50(4):445–478, 2012.
49. D. Schillinger, L. Dede', M.A. Scott, J.A. Evans, M.J. Borden, E. Rank, and T.J.R. Hughes. An isogeometric design-through-analysis methodology based on adaptive hierarchical refinement of NURBS, immersed boundary methods, and T-spline CAD surfaces. *Computer Methods in Applied Mechanics and Engineering*, 249-250:116–150, 2012.
50. S. Duczek and U. Gabbert. The finite cell method for polygonal meshes: poly-FCM. *Computational Mechanics*, 58:587–618, 2016.
51. A. Hansbo and P. Hansbo. An unfitted finite element method, based on Nitsche's method, for elliptic interface problems. *Computer Methods in Applied Mechanics and Engineering*, 191:537–552, 2002.
52. A. Embar, J. Dolbow, and I. Harari. Imposing Dirichlet boundary conditions with Nitsche's method and spline-based finite elements. *International Journal for Numerical Methods in Engineering*, 83:877–898, 2010.
53. M. Ruess, D. Schillinger, Y. Bazilevs, V. Varduhn, and E. Rank. Weakly enforced essential boundary conditions for NURBS-embedded and trimmed NURBS geometries on the basis of the finite cell method. *International Journal for Numerical Methods in Engineering*, 95(10):811–846, 2013.
54. D. Schillinger, I. Harari, M.-C. Hsu, D. Kamensky, K.F.S. Stoter, Y. Yu, and Z. Ying. The non-symmetric Nitsche method for the parameter-free imposition of weak boundary and coupling conditions in immersed finite elements. *Computer Methods in Applied Mechanics and Engineering*, 309:625–652, 2016.
55. P. Keast. Moderate-degree tetrahedral quadrature formulas. *Computer Methods in Applied Mechanics and Engineering*, 55:339–348, 1986.
56. F.H. Fenton, E.M. Cherry, A. Karma, and W.-J. Rappel. Modeling wave propagation in realistic heart geometries using the phase-field method. *Chaos: An Interdisciplinary Journal of Nonlinear Science*, 15(1):013502, 2005.
57. X. Chen. Generation, propagation, and annihilation of metastable patterns. *Journal of Differential Equations*, 206(2):399–437, 2004.
58. J. Carr and R.L. Pego. Metastable patterns in solutions of $u_t = \varepsilon 2u_{xx} - f(u)$. *Communications on Pure and Applied Mathematics*, 42(5):523–576, 1989.
59. J. Shen and X. Yang. Numerical approximations of Allen-Cahn and Cahn-Hilliard equations. *Discrete and Continuous Dynamical Systems*, 28(4):1669–1691, 2010.
60. W. Birkfellner. *Applied Medical Image Processing: A Basic Course*. Taylor & Francis, 2014.
61. D. Schillinger, L.H. Nguyen, S.K.F. Stoter, and M. Sanchez Uribe. The diffuse Nitsche method: phase-field based imposition of Dirichlet boundary conditions. *in preparation*.
62. V. Nübel. *Die adaptive rp-Methode für elastoplastische Probleme*. Dissertation, Technische Universität München, 2005.
63. D. Schillinger, J.A. Evans, F. Frischmann, R.R. Hiemstra, M.-C. Hsu, and T.J.R. Hughes. A collocated C^0 finite element method: Reduced quadrature perspective, cost comparison with standard finite elements, and explicit structural dynamics. *International Journal for Numerical Methods in Engineering*, 102(3-4):576–631, 2015.
64. E. Schileo, E. Dall'Ara, F. Taddei, A. Malandrino, T. Schotkamp, M. Baleani, and M. Viceconti. An accurate estimation of bone density improves the accuracy of subject-specific finite element models. *Journal of Biomechanics*, 41(11):2483–2491, 2008.
65. F. Taddei, M. Pani, L. Zovatto, E. Tonti, and M. Viceconti. A new meshless approach for subject-specific strain prediction in long bones: Evaluation of accuracy. *Clinical Biomechanics*, 23(9):1192–1199, 2008.
66. P.H.F. Nicholson, X.G. Cheng, G. Lowet, S. Boonen, M.W.J. Davie, J. Dequeker, and G. Van der Perre. Structural and material mechanical properties of human vertebral cancellous bone. *Medical Engineering & Physics*, 19(8):729–737, 1997.
67. M. Schlottbom. Error analysis of a diffuse interface method for elliptic problems with Dirichlet boundary conditions. *arXiv preprint arXiv:1507.08814v2*, 2016.